Research Square

Preprints are preliminary reports that have not undergone peer review.
They should not be considered conclusive, used to inform clinical practice,
or referenced by the media as validated information.

Thermomechanical modelling of concrete with aggregate inclusions using total Lagrangian B-spline material point method

Haitao Ding
Jiangxi University of Science and Technology
Zheng Sun
Jiangxi University of Science and Technology
Weiling Xiao
Jiangxi University of Science and Technology
Xiaomin Zhou
xmzhou@jxust.edu.cn

Jiangxi University of Science and Technology

Research Article

Keywords:

Posted Date: November 16th, 2026

DOI: https://doi.org/10.21203/rs.3.rs-11616577/v1

License: This work is licensed under a Creative Commons Attribution 4.0 International License.
Read Full License

Additional Declarations: No competing interests reported.

Thermomechanical modelling of concrete with aggregate inclusions using total Lagrangian B-spline material point method

Haitao Ding[a], Zheng Sun[a], Weiling Xiao[a], Xiaomin Zhou[a,b,*]

[a] *Jiangxi Provincial Key Laboratory of Environmental Geotechnical Engineering and Disaster Control, Jiangxi University of Science and Technology, Ganzhou, 341000, China*
[b] *CAS Key Laboratory of Mechanical Behavior and Design of Materials, Department of Modern Mechanics, University of Science and Technology of China, Jinzhai, Hefei, 230027, Anhui, China*

Abstract

Concrete with aggregate inclusions exhibit coupled heat transfer, stress-wave propagation, and damage across mortar, aggregates, and interfacial transition zones. This study develops a total Lagrangian B-spline material point method (TLBSMPM) for coupled mechanical and thermal analysis, with interpolation fixed in the reference configuration. We assess the method using elastic-wave and bending benchmarks, a heat-conduction test, a thermally shocked cantilever, and impact simulations of homogeneous and three-phase concrete disks. For TLBSMPM, errors decrease with grid refinement in the wave and heat-conduction tests, and the cantilever frequency agrees with beam theory within 0.75%. In bending, total Lagrangian methods reduce stress oscillations and computation time relative to updated Lagrangian methods at the same grid size. Wave accuracy depends on particle arrangement: linear interpolation performs better for uniform particles, whereas cubic B-splines perform better for the tested nonuniform arrangement. In the three-phase disks, damage concentrates in and around the interfaces. The ranking of mass-weighted global damage changes over time; because undamaged aggregate mass remains in the average, this measure does not compare damage only in mortar and interfaces. These results support phase-resolved thermomechanical analysis under the tested conditions.

*Corresponding author. Email: xmzhou@jxust.edu.cn. ORCID iD: 0000-0003-2886-5447.
Email addresses: 6720240502@mail.jxust.edu.cn (Haitao Ding), sunzheng@jxust.edu.cn (Zheng Sun), 9120160068@jxust.edu.cn (Weiling Xiao), xmzhou@jxust.edu.cn (Xiaomin Zhou)

Keywords: B-spline material point method, total Lagrangian formulation, concrete with aggregate inclusions, thermomechanical modelling, interfacial transition zone

1. Introduction

Thermomechanical modelling of concrete with aggregate inclusions requires distinct descriptions of mortar, aggregates and interfacial transition zones (ITZs). Constituent properties and loading history govern the computed stress and damage under temperature changes and transient loading.

Ma et al. [1] reviewed the temperature dependence of concrete's mechanical properties, whereas Manzoor et al. [2] examined elevated-temperature performance in geopolymer concrete. These reviews show the importance of mixture composition when interpreting concrete's response to temperature. Their different binder systems limit the direct transfer of temperature-dependent constitutive descriptions between concretes. Studies of penetration followed by explosion and of embedded explosions show that concrete damage depends on loading sequence and location [3, 4]. Thermal experiments examine distinct physical processes relevant to thermomechanical modelling. Li et al. [5] measured early-age deformation and thermal expansion, while Bangi and Horiguchi [6] investigated pore pressure in heated fibre-reinforced high-strength concrete. These measurements constrain different parts of a thermomechanical model, neither alone determines the evolution of local damage around an aggregate. Recent studies have also addressed transient heat-transfer problems relevant to concrete and heterogeneous materials. Bu et al. [7] investigated the identification of the hydration-heat source in concrete, Li et al. [8] developed a framework for transient nonlinear and inhomogeneous heat conduction, and Bidou et al. [9] considered a two-dimensional transient inverse heat-conduction problem with static and moving heat sources. These studies highlight the importance of transient thermal-field prediction, but they mainly focus on thermal prediction or source identification rather than on the simultaneous phase-resolved treatment of heat transfer, stress waves and damage. Spalling analyses account for transport and fracture, in addition to thermal strain, through coupled and cohesive-interface formulations [10, 11]. At the constituent scale, Kong et al. [12] investigated microstructure evolution in the ITZ between an alkali-activated fly ash/slag matrix and aggregate, providing experimental context for explicit interface representation. These studies support phase-resolved modelling, with separate assessments of thermal transport, mechanical response and constitutive behaviour.

Existing concrete models represent heterogeneity at different scales, and validation applies to the processes resolved at each scale. Kashif et al. [13] used

finite elements to examine temperature-induced cracking in actively reinforced concrete pavement slabs. Their model represented structural restraint and thermal loading without resolving individual aggregate inclusions. At the mesoscale, Chen et al. [14] developed a strength-grade-adaptive aggregate-generation method using multientropy-multifractal optimisation for refined concrete finite-element modelling, highlighting the role of aggregate geometry in mesoscale model construction. Recent studies in building engineering have further shown that aggregate morphology, ITZ properties and phase-dependent thermal properties can affect heat conduction, thermal-stress development and damage localisation in concrete [15–17]. These results support the explicit representation of concrete constituents in a phase-aware model, while the present work additionally examines particle–grid transfer accuracy and coupled mechanical response. This approach reduces the cost of constituent modelling and reproduces uniaxial and biaxial strength data. The present work extends mesoscale modelling to transient heat transport and particle–grid stress transfer. Tordesillas et al. [18] analysed force-transmission networks in discrete-element concrete specimens to identify potential macrocrack locations before peak load. Their analysis relates load-path distribution and bond failure to damage, supporting damage measures with phase and spatial resolution. Fracture experiments by Mutnbak et al. [19] show that comparisons of damage or fracture measures must account for specimen geometry and size. The parameter study of Ren et al. [20] shows that the Holmquist–Johnson–Cook (HJC) model requires material-specific calibration. Impact studies have characterised concrete damage across multiple length scales, evaluated dynamic constitutive models, and numerically examined impact-loaded young concrete prisms [21–23]. Together, these studies show that constitutive modelling and loading conditions shape the interpretation of concrete impact response.

Material point methods (MPM) store constituent identities and material histories on particles and solve balance equations on a background grid [24–26]. Particle–grid transfer introduces numerical errors that must be assessed separately from constitutive behaviour. Steffen et al. [27, 28] analysed quadrature errors and implementation choices, showing that particle integration and transfer affect accuracy in addition to spatial approximation. Generalised interpolation gives particles finite support [29], while convected particle-domain interpolation follows domain deformation and can represent weak discontinuities through enrichment [30, 31]. These methods modify particle-domain representation, whereas basis regularity and integration accuracy have distinct numerical effects. Gan et al. [32] combined B-spline interpolation with improved quadrature to reduce cell-crossing errors and improve impact calculations. The resulting stress histories depend on

both the basis and the quadrature. The choice of reference or current configuration also affects transfer operations. The total Lagrangian formulation of de Vaucorbeil et al. [33] evaluates particle support in material coordinates, allowing reference weights and gradients to be reused. Telikicherla and Moutsanidis [34] assessed higher-order bases and near-incompressibility as separate aspects of numerical performance. Contact and phase-field extensions allow reference-based MPM to represent additional mechanical processes [35–37]. For coupled problems, Tao et al. [38] formulated thermomechanical GIMP, and Lee and Shin [39] developed a corotated total Lagrangian SPH formulation for elastic bodies. Physics-informed approaches address weakly and fully coupled transient thermomechanics [40]. These formulations use different treatments of the coupled equations, requiring controlled comparisons of MPM basis continuity, transfer configuration and particle distribution. Heat transport in the reference configuration maintains consistency between the conductivity pull-back, kinematics and thermal balance [41]. This study evaluates fixed-reference B-spline transfer for thermomechanical modelling of concrete with aggregate inclusions. Mechanical benchmarks and separate thermal tests distinguish interpolation and quadrature effects from constitutive behaviour within the tested conditions.

Taken together, the available studies do not yet provide a single particle-based mesoscale framework that simultaneously resolves phase-specific heat transfer, stress-wave propagation, particle–grid transfer accuracy and damage localisation in concrete with aggregate inclusions. In this work, we formulate total Lagrangian B-spline MPM (TLBSMPM) with reusable material-coordinate support and a material-coordinate heat balance. The multiharmonic travelling-wave benchmark compares four transfer schemes under uniform drift and a prescribed nonuniform particle quadrature. Pure bending of an elastic beam assesses axial stress accuracy, stress oscillations and computational cost. Slab heat conduction is compared with an analytical solution, and the fundamental frequency of a thermally shocked cantilever is compared with beam theory. The disk example compares coupled temperature, stress and damage fields in one homogeneous and four three-phase concrete models.

Section 2 presents B-spline reference support, mechanical transfer, thermomechanical coupling, phase-resolved response measures and the disk constitutive model. Section 3 reports the travelling-wave, bending, slab, beam and disk examples. Section 4 examines how basis continuity, reference-map reuse and particle distribution affect stress accuracy and computational cost. Section 5 summarises the main findings and their limits of applicability.

2. Numerical framework

The framework couples mechanical and thermal balances using shared B-spline interpolation in the reference configuration. Mortar, aggregates and ITZs retain distinct material properties, while fixed interpolation weights and gradients are reused throughout the calculation.

2.1. Total Lagrangian B-spline Material Point Method (TLBSMPM)

The reference domain is partitioned into mortar, aggregate and ITZ regions,

$$\Omega_0 = \Omega_0^{\mathrm{m}} \cup \Omega_0^{\mathrm{a}} \cup \Omega_0^{\mathrm{i}}, \qquad \chi_p \in \{\mathrm{m}, \mathrm{a}, \mathrm{i}\}. \tag{1}$$

The interiors of the three material regions do not overlap. Every particle retains its phase label χ_p, reference volume, mass and phase-specific material coefficients. Each ITZ is represented as a material region of finite thickness. Phase labels are retained during transfer, although nodal quantities sum contributions from all supported particles. Constitutive and conductivity calculations use the properties assigned to each particle.

The total Lagrangian B-spline material point method (TLBSMPM) stores mass and constitutive history on material points. Discrete balance equations are solved on a tensor-product B-spline grid defined in the initial configuration. Particle positions, velocities, deformation gradients, stresses and temperatures evolve with time. Each particle's reference position fixes its interpolation support for mechanical and thermal transfer. The reference weights and gradients are evaluated once and reused throughout the calculation.

Let $\boldsymbol{X} \in \Omega_0$ denote the material coordinate and $\boldsymbol{x} = \boldsymbol{\varphi}(\boldsymbol{X}, t)$ the current position. The deformation gradient, Jacobian and spatial velocity gradient are

$$\boldsymbol{F} = \frac{\partial \boldsymbol{x}}{\partial \boldsymbol{X}}, \qquad J = \det \boldsymbol{F} > 0, \qquad \boldsymbol{L} = \dot{\boldsymbol{F}}\boldsymbol{F}^{-1}. \tag{2}$$

Under the kinematics in Eq. (2), mass conservation gives $\rho J = \rho_0$. A particle has fixed mass m_p and reference volume $V_p^0 = m_p/\rho_{0p}$; its current volume is $J_p V_p^0$. The reference momentum balance uses the first Piola–Kirchhoff stress $\boldsymbol{P}$:

$$\rho_0 \ddot{\boldsymbol{x}} = \mathrm{Div}_{\boldsymbol{X}}\, \boldsymbol{P} + \rho_0 \boldsymbol{b}, \qquad \boldsymbol{P} = J\boldsymbol{\sigma}\boldsymbol{F}^{-\mathsf{T}}, \tag{3}$$

where $\boldsymbol{\sigma}$ is Cauchy stress and $\boldsymbol{b}$ is body force per unit mass.

The basis is defined on a knot vector, a nondecreasing sequence of knot coordinates in the parameter domain,

$$\boldsymbol{\Xi} = \{\xi_1, \xi_2, \ldots, \xi_{n+q+1}\}, \tag{4}$$

where ξ_i is the ith knot, n is the number of basis functions and q is the polynomial degree. Two adjacent unequal knots delimit a knot span, and a knot vector is uniform when every span has the same length and nonuniform otherwise. A knot that occurs k times has multiplicity k. Bounded problems use open knot vectors, in which the first and last knots each occur $q + 1$ times,

$$\xi_1 = \cdots = \xi_{q+1}, \qquad \xi_{n+1} = \cdots = \xi_{n+q+1}. \tag{5}$$

The degree-q basis then follows the Cox–de Boor recurrence:

$$N_{i,0}(\xi) = \begin{cases} 1, & \xi_i \le \xi < \xi_{i+1}, \\ 0, & \text{otherwise}, \end{cases} \tag{6}$$

$$N_{i,q}(\xi) = \frac{\xi - \xi_i}{\xi_{i+q} - \xi_i} N_{i,q-1}(\xi) + \frac{\xi_{i+q+1} - \xi}{\xi_{i+q+1} - \xi_{i+1}} N_{i+1,q-1}(\xi). \tag{7}$$

A zero-denominator term in Eq. (7) is set to zero, with a one-sided limit at the final endpoint of Eq. (6). Figure 1 summarises the recursion, and Figure 2 shows the first- and third-degree bases on $[0, 1]$. At simple interior knots, cubic functions have C^2 continuity and linear functions have C^0 continuity. An open knot vector also makes the basis interpolatory at the two endpoints, where one function equals unity and all others vanish. Tensor products define $N_I(\boldsymbol{X})$ in multiple dimensions, with derivatives accounting for the transformation from parametric to material coordinates.

The reference weights and gradients are

$$w_{Ip} = N_I(\boldsymbol{X}_p), \qquad \boldsymbol{G}_{Ip} = \mathrm{Grad}_{\boldsymbol{X}}\, N_I(\boldsymbol{X}_p), \qquad \sum_I w_{Ip} = 1, \quad \sum_I \boldsymbol{G}_{Ip} = \boldsymbol{0}. \tag{8}$$

The support set, w_{Ip} and $\boldsymbol{G}_{Ip}$ are evaluated once and reused. Fixed-reference interpolation determines connectivity, while basis degree determines approximation regularity [32, 33]. A cubic tensor product has up to 16 supported nodes per particle in two dimensions and 64 in three dimensions. For N_p particles and s supported nodes, storage requirements and transfer cost scale as $O(N_p s)$. Open knot vectors are used for all bounded problems in this study. The linear TLMPM control changes the basis degree while retaining the reference geometry, particle quadrature and update sequence.

The mechanical cycle transfers particle mass and momentum to the grid and assembles nodal forces. Nodal accelerations update particle motion, and remapped

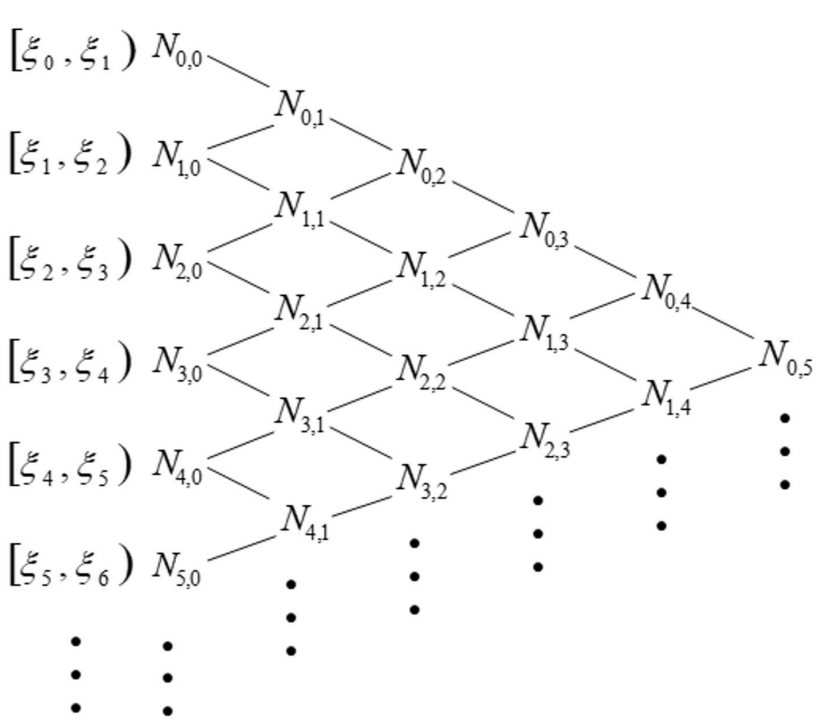


Figure 1: Cox–de Boor recursion for B-spline basis functions.

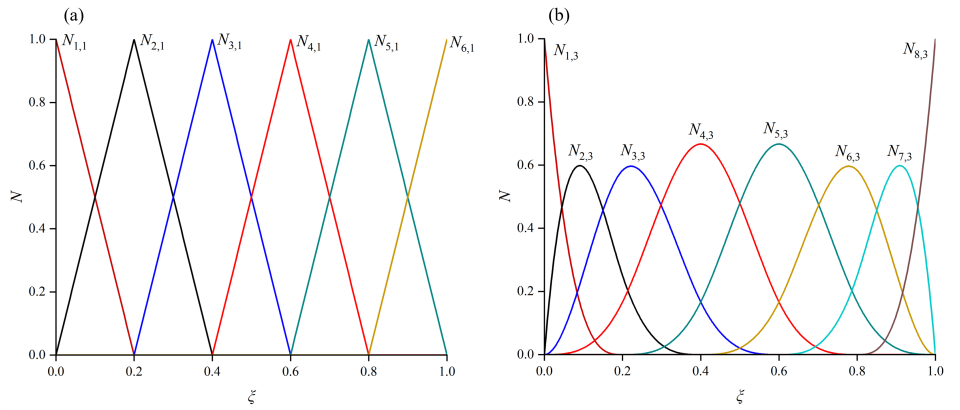


Figure 2: B-spline basis functions on $[0, 1]$: (a) linear basis; (b) cubic basis.

velocities provide the material velocity gradient for deformation and stress evolution. The following equations define the mechanical cycle, and Section 2.2 describes thermal coupling using the same reference support.

Applying the weak form of Eq. (3) and particle quadrature gives lumped nodal mass, momentum and internal force:

$$m_I = \sum_p m_p w_{Ip}, \qquad \boldsymbol{q}_I^n = \sum_p m_p w_{Ip} \boldsymbol{v}_p^n, \tag{9}$$

$$\boldsymbol{f}_I^{\mathrm{int},n} = -\sum_p V_p^0 \boldsymbol{P}_p^n \boldsymbol{G}_{Ip}, \qquad \boldsymbol{a}_I^n = \frac{\boldsymbol{f}_I^{\mathrm{int},n} + \boldsymbol{f}_I^{\mathrm{ext},n}}{m_I}. \tag{10}$$

The external force in Eq. (10) includes body forces and reference tractions. Using the mapped momentum in Eq. (9), the explicit active-node velocity is $\boldsymbol{v}_I^\star = \boldsymbol{q}_I^n/m_I + \Delta t\, \boldsymbol{a}_I^n$. Particle velocities and positions are updated as

$$\boldsymbol{v}_p^{n+1} = \boldsymbol{v}_p^n + \Delta t \sum_I w_{Ip} \boldsymbol{a}_I^n, \qquad \boldsymbol{x}_p^{n+1} = \boldsymbol{x}_p^n + \Delta t \sum_I w_{Ip} \boldsymbol{v}_I^\star. \tag{11}$$

Following Eq. (11), the modified update stress last (MUSL) cycle remaps updated particle velocities:

$$\widetilde{\boldsymbol{v}}_I = \frac{\sum_p m_p w_{Ip} \boldsymbol{v}_p^{n+1}}{m_I}, \qquad \boldsymbol{H}_p = \sum_I \widetilde{\boldsymbol{v}}_I \otimes \boldsymbol{G}_{Ip}. \tag{12}$$

After reimposing essential velocity conditions, $\boldsymbol{H}_p$ in Eq. (12) approximates the material velocity gradient. The kinematic update is

$$\boldsymbol{F}_p^{n+1} = \boldsymbol{F}_p^n + \Delta t\, \boldsymbol{H}_p, \qquad \boldsymbol{L}_p = \boldsymbol{H}_p (\boldsymbol{F}_p^{n+1})^{-1}. \tag{13}$$

Equation (13) advances deformation while reference volumes remain in the internal-force assembly. The constitutive calculation supplies the Cauchy stress used in the Piola transformation.

The implementation follows the standard material-point cycle with the reference support fixed at initialisation. Each particle receives a phase label, reference volume, mass and initial state. The weights, gradients and support sets of Eq. (8) are then evaluated from the initial particle positions and stored. Each time step transfers mass and momentum, assembles nodal forces, updates particle motion and remaps velocities to obtain the material velocity gradient. Deformation follows Eq. (13), and the stress update uses the constitutive law assigned to each phase. The

thermal branch transfers heat capacity and heat rate, updates particle temperatures and reconstructs nodal temperatures through Eq. (19).

The updated Lagrangian B-spline material point method (ULBSMPM) evaluates support in the current configuration at every step. TLBSMPM reuses reference support, with interpolation weights and gradients remaining unchanged as particles move across grid cells. Algorithm 1 summarises the thermomechanical cycle and the associated response measures.

2.2. Thermomechanical coupling in TLBSMPM

Thermoelastic coupling is represented by thermal strain in the constitutive update and deformation-dependent conductivity in the heat balance. For isotropic thermoelastic response, the local small-strain relation is given by

$$\boldsymbol{\sigma} = \mathbb{C} : [\boldsymbol{\varepsilon} - \alpha_T(T - T_0)\boldsymbol{I}], \tag{14}$$

where α_T is the linear expansion coefficient. Equation (14) relates stress to the full temperature difference $T - T_0$, and its rate form uses the objective stress rate, the strain rate sym $\boldsymbol{L}$ and the thermal strain rate.

The pure-bending and thermally shocked cantilever benchmarks use small-strain isotropic elasticity. The slab benchmark isolates heat conduction. Under plane strain, $\varepsilon_{zz} = 0$ but σ_{zz} is generally nonzero:

$$\begin{aligned}
\sigma_{xx,p} &= (\lambda_p + 2\mu_p)\varepsilon_{xx,p} + \lambda_p\varepsilon_{yy,p} - \beta_p\theta_p, \\
\sigma_{yy,p} &= \lambda_p\varepsilon_{xx,p} + (\lambda_p + 2\mu_p)\varepsilon_{yy,p} - \beta_p\theta_p, \\
\sigma_{xy,p} &= \mu_p\gamma_{xy,p}, \qquad \sigma_{zz,p} = \lambda_p(\varepsilon_{xx,p} + \varepsilon_{yy,p}) - \beta_p\theta_p, \\
\beta_p &= (3\lambda_p + 2\mu_p)\alpha_{T,p}, \qquad \theta_p = T_p - T_0.
\end{aligned} \tag{15}$$

Here $\gamma_{xy} = 2\varepsilon_{xy}$ denotes the engineering shear strain at each material point. The MUSL remap supplies the strain rate used to calculate the strain increment. The thermal stress increment uses the complete $\Delta\theta_p$ applied during that step. This small-strain approximation sets $\boldsymbol{P} \approx \boldsymbol{\sigma}$ in the force assembly for the elastic beam benchmarks. The disk uses phase-specific constitutive laws, including the HJC model of Section 2.4 for mortar and ITZ.

Heat transport is written in the same reference coordinates. The spatial Fourier law $\boldsymbol{q} = -\boldsymbol{k}\nabla_{\boldsymbol{x}}T$ transforms to

$$\boldsymbol{Q} = J\boldsymbol{F}^{-1}\boldsymbol{q} = -\boldsymbol{K}_0 \operatorname{Grad}_{\boldsymbol{X}} T, \qquad \boldsymbol{K}_0 = J\boldsymbol{F}^{-1}\boldsymbol{k}\boldsymbol{F}^{-\mathsf{T}}. \tag{16}$$

For positive J and symmetric positive-definite $\boldsymbol{k}$, $\boldsymbol{K}_0$ is positive definite. An isotropic spatial material, $\boldsymbol{k} = k\boldsymbol{I}$, generally has an anisotropic reference tensor.

The finite-deformation form in Eq. (16) uses the current deformation gradient, while the reference interpolation weights and gradients remain fixed. Its small-deformation approximation takes $\boldsymbol{F} \approx \boldsymbol{I}$, $J \approx 1$ and $\boldsymbol{K}_0 \approx k\boldsymbol{I}$.

For constant specific heat c, the reference thermal balance is

$$\rho_0 c \dot{T} = \mathrm{Div}_{\boldsymbol{X}}(\boldsymbol{K}_0 \,\mathrm{Grad}_{\boldsymbol{X}}\, T) + R_0 + R_{\mathrm{te},0} + R_{\mathrm{p},0}. \tag{17}$$

In Eq. (17), R_0 is prescribed heat input, $R_{\mathrm{te},0}$ is reversible thermoelastic exchange, and $R_{\mathrm{p},0}$ is an inelastic heat source. The stress-power expression $R_{\mathrm{p},0} = \chi J \boldsymbol{\sigma} : \boldsymbol{D}^{\mathrm{p}}$ uses the conversion fraction χ and plastic rate $\boldsymbol{D}^{\mathrm{p}}$ [41].

Capacity-weighted particle–grid transfer uses

$$C_I = \sum_p m_p c_p w_{Ip}, \qquad r_I = \sum_p V_p^0 \left(\boldsymbol{G}_{Ip} \cdot \boldsymbol{Q}_p + w_{Ip} R_{0p}^{\mathrm{tot}} \right) + r_I^{\mathrm{b}}, \tag{18}$$

where R_0^{tot} collects the volumetric sources and r_I^{b} is incoming boundary heat. The explicit particle update and capacity-weighted temperature reconstruction are

$$\dot{T}_p = \sum_{I:C_I>0} w_{Ip} \frac{r_I}{C_I}, \qquad T_p^\star = T_p^n + \Delta t\, \dot{T}_p, \qquad T_I = \frac{\sum_p m_p c_p w_{Ip} T_p}{C_I}. \tag{19}$$

Prescribed temperatures complete the particle update in Eq. (19). Summing Eq. (18) over nodes cancels internal flux contributions through Eq. (8). The resulting heat balance contains only external heating and volumetric sources.

2.3. Phase-resolved response and damage measures

Temperature rise, reference heat flux, displacement, velocity and stress describe the mechanical and thermal response. Phase labels allow these quantities to be resolved within mortar, aggregates and ITZs in the heterogeneous disk. The phase reference-volume fraction and reference thermal energy are

$$f_\chi^0 = \frac{\sum_{p:\chi_p=\chi} V_p^0}{\sum_p V_p^0}, \qquad E_\theta = \sum_p m_p c_p (T_p - T_0). \tag{20}$$

The fractions in Eq. (20) describe the discretised phase composition. The assembled heat and momentum balances are used to check conservation. Analytical reference fields are used to evaluate accuracy in the benchmark problems.

The bending stress and slab temperature benchmarks use the relative discrete L_2 error

$$e_u(t) = \left[\frac{\sum_{p\in\mathcal{S}} \|\boldsymbol{u}_p^{\mathrm{num}}(t) - \boldsymbol{u}_p^{\mathrm{ref}}(t)\|^2}{\sum_{p\in\mathcal{S}} \|\boldsymbol{u}_p^{\mathrm{ref}}(t)\|^2} \right]^{1/2}. \tag{21}$$

Here $\mathcal{S}$ is the particle set specified for each benchmark, and numerical and reference fields are sampled at the same particle locations. The norm denotes absolute value for a scalar and the Euclidean norm for a vector; the reference denominator must be nonzero. Equation (21) uses unweighted particle sums. The travelling-wave benchmark uses a separate volume-weighted error with a fixed analytical scale, defined in Section 3.1.

Local equivalent stress is $\sigma_{\mathrm{eq}} = (3\boldsymbol{s} : \boldsymbol{s}/2)^{1/2}$, with deviatoric stress $\boldsymbol{s} = \operatorname{dev}\boldsymbol{\sigma}$. Each material point carries its phase-specific state and damage variable D_p. The mass-weighted global damage is

$$D_{\mathrm{global}}(t) = \frac{\sum_p m_p D_p(t)}{\sum_p m_p}. \tag{22}$$

If aggregate damage is zero, let $w_{\mathrm{a}} = \sum_{p:\chi_p=\mathrm{a}} m_p / \sum_p m_p$ denote the aggregate mass fraction. The mass-weighted mean damage in mortar and ITZ is $\bar{D}_{\mathrm{d}}$, giving

$$D_{\mathrm{global}} = (1 - w_{\mathrm{a}})\bar{D}_{\mathrm{d}}, \qquad \bar{D}_{\mathrm{d}} = \frac{\sum_{p\in\{\mathrm{mortar,ITZ}\}} m_p D_p}{\sum_{p\in\{\mathrm{mortar,ITZ}\}} m_p}. \tag{23}$$

Equation (22) uses the total particle mass, while $\bar{D}_{\mathrm{d}}$ in Eq. (23) uses only the mass of mortar and ITZ. The identity separates the damage state of these phases from their contribution to the total mass.

2.4. HJC constitutive model

The disk example of Section 3.5 uses the Holmquist–Johnson–Cook (HJC) model for mortar and ITZ. Aggregates follow an elastic–plastic constitutive law that excludes damage evolution. The three components of the HJC model are summarised below. Here σ^* denotes normalised equivalent stress and p denotes hydrostatic pressure, distinct from the Piola stress $\boldsymbol{P}$. The symbol T^* denotes normalised tensile strength and is distinct from temperature.

The strength model combines strain-rate strengthening with pressure hardening,

$$\sigma^* = \left[A(1 - D) + Bp^{*N}\right](1 + C\ln\dot{\varepsilon}^*), \tag{24}$$

where $\sigma^* = \sigma_{\mathrm{eq}}/f_c'$ and $p^* = p/f_c'$ are normalised by the reference strength f_c'. The dimensionless strain rate is $\dot{\varepsilon}^* = \dot{\varepsilon}/\dot{\varepsilon}_0$, where $\dot{\varepsilon}_0$ is the reference strain rate. A is the normalised cohesive strength, B the pressure-hardening coefficient and N the pressure-hardening exponent. The parameters C and D denote strain-rate sensitivity and damage, respectively.

The equation of state describes volumetric compaction through three branches,

$$p = \begin{cases} K\mu, & U \le U_{\text{crush}}, \\ p_{\text{crush}} + K_{\text{lock}}\left(\mu - \mu_{\text{crush}}\right), & U_{\text{crush}} < U < U_{\text{lock}}, \\ K_1\bar{\mu} + K_2\bar{\mu}^2 + K_3\bar{\mu}^3, & U \ge U_{\text{lock}}, \end{cases} \tag{25}$$

where K is the bulk modulus, K_{lock} the compaction modulus of the transition branch, p_{crush} the elastic-limit pressure, and K_1, K_2 and K_3 pressure constants. The variables U, U_{crush} and U_{lock} denote current volumetric compression, its elastic limit and its value at full pore compaction. The variables μ, μ_{crush} and $\bar{\mu}$ are the corresponding volumetric strains. The crush and lock thresholds define transitions between the three branches of the equation of state.

The damage model accumulates equivalent plastic and plastic volumetric strain,

$$D = \sum \frac{\Delta\varepsilon_p + \Delta\mu_p}{\varepsilon_p^f + \mu_p^f}, \tag{26}$$

with the failure strain

$$\varepsilon_p^f + \mu_p^f = D_1\left(p^* + T^*\right)^{D_2} \ge \text{EFMIN}, \tag{27}$$

where $\Delta\varepsilon_p$ and $\Delta\mu_p$ are the equivalent plastic and plastic volumetric strain increments within one step. The sum $\varepsilon_p^f + \mu_p^f$ is the accumulated plastic strain at complete failure. $T^* = T/f_c'$ denotes the normalised maximum tensile stress, and D_1 and D_2 are damage parameters. The parameter EFMIN specifies the minimum accumulated strain required for failure.

The elastic beam benchmarks use Eq. (15), while the slab benchmark tests heat conduction without constitutive damage. The travelling-wave benchmark defines its own elastic law in Section 3.1.

Algorithm 1 summarises phase-resolved preprocessing, mechanical transfer, thermal updating and constitutive calculations. It also specifies evaluation of the response measures defined in Section 2.3.

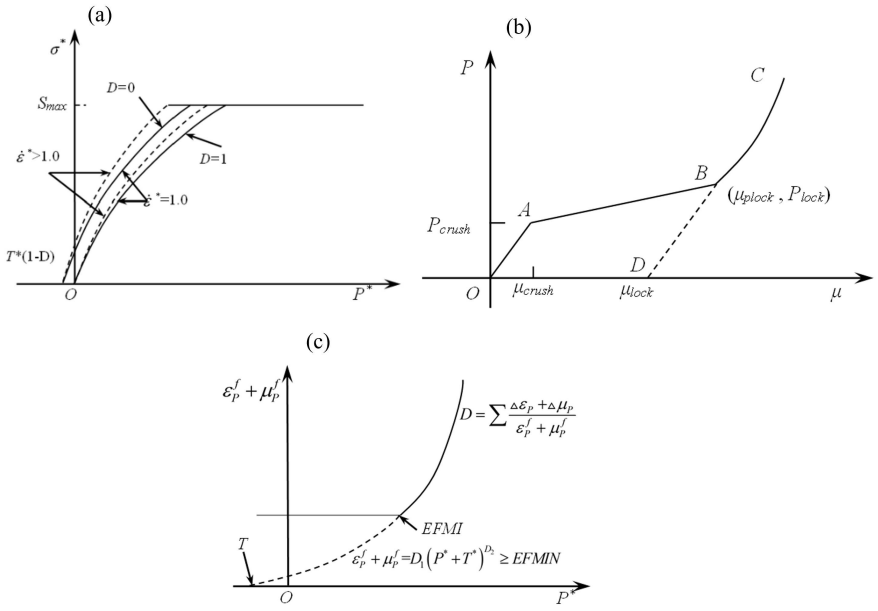


Figure 3: HJC constitutive model for mortar and ITZ: (a) strength model; (b) equation of state; (c) damage model.

Algorithm 1 Phase-resolved TLBSMPM thermomechanical cycle and response measures.

Require: Particle data $\{\boldsymbol{X}_p, m_p, V_p^0, \chi_p, \boldsymbol{F}_p^0, \boldsymbol{v}_p^0, T_p^0\}$, reference grid and knot vector $\boldsymbol{\Xi}$, phase coefficients $\{\lambda_p, \mu_p, \alpha_{T,p}, c_p, \boldsymbol{K}_{0p}\}$, observation times $\mathcal{T}$

Preprocessing

Partition the reference domain into mortar, aggregate and ITZ regions and discretise it into phase-labelled particles (Eq. (1))

Evaluate w_{Ip} and $\boldsymbol{G}_{Ip}$ once from Eq. (8), store the support sets and assemble the nodal masses

Assemble the initial particle stresses from Eqs. (14) and (15)

Thermomechanical cycle

for $n = 0$ to $n_{\text{end}} - 1$ **do**

    Map mass, momentum and internal forces to the active nodes and form the nodal accelerations (Eqs. (9) and (10))

    Update the particle velocities and positions and reimpose the essential velocity conditions (Eq. (11))

    Remap the velocities to obtain the material velocity gradient (Eq. (12)) and advance the deformation and velocity gradients (Eq. (13))

    if the case uses the thermoelastic benchmark law **then**

        Update the phase-wise stress with the temperature increment and the plane-strain closure (Eqs. (14) and (15))

    else

        Update mortar and ITZ with the HJC model (Eqs. (24)–(27)); update aggregates with their elastic–plastic law

    end if

    Pull the conductivity back to the reference configuration and transfer heat capacity and heat rate (Eqs. (16) and (18))

    Update the particle temperatures, reconstruct the nodal temperatures and impose the prescribed boundary temperatures (Eq. (19))

end for

Observables

for each $t \in \mathcal{T}$ **do**

    Evaluate the applicable response measures and benchmark errors using their case-specific definitions

    Evaluate global and damageable-phase mean damage using Eqs. (22) and (23)

end for

3. Numerical examples

Five numerical examples assess the accuracy, computational cost and thermomechanical predictions of TLBSMPM. Travelling-wave and pure-bending benchmarks compare four material point formulations, while slab conduction and cantilever vibration under thermal shock are assessed against analytical references. Impact loading of homogeneous and three-phase concrete disks examines coupled temperature, stress and damage evolution.

3.1. Multiharmonic travelling wave

This benchmark compares four transfer schemes for a periodic one-dimensional elastic wave containing eight spatial harmonics. Three prescribed particle and drift configurations are tested over five wave transits. The analytical solution provides a common reference for assessing stress error, waveform evolution and computational cost.

Consider one period, $0 \le X < L$, of an infinite one-dimensional elastic medium with unit cross-sectional area, as shown in Figure 4(a). The parameters are $L = 1$ m, $E = 10$ MPa and $\rho_0 = 1000\,\mathrm{kg\,m^{-3}}$, giving wave speed $c_0 = \sqrt{E/\rho_0} = 100\,\mathrm{m\,s^{-1}}$ and transit time $T_\mathrm{w} = L/c_0 = 0.01$ s. A uniform drift velocity V is added to the travelling-wave motion:

$$\begin{gathered} x(X,t) = X + Vt + u(X,t), \qquad F = x_{,X}, \\ W(F) = \tfrac{1}{2}E(F-1)^2, \qquad P = E(F-1), \qquad \rho_0 x_{,tt} = P_{,X}. \end{gathered} \tag{28}$$

Equation (28) defines the one-dimensional elastic material used for the benchmark. Body forces, damping, thermal loading and damage are absent. The end faces are periodic. The fields u, v, F and P are periodic, while the motion satisfies $x(X + L, t) = x(X, t) + L$.

Define the fixed spectral weights and phase by

$$w_m = \exp\!\left[-\frac{1}{2}\left(\frac{m-4}{1.5}\right)^2\right], \quad S = \sum_{m=1}^{8} w_m, \quad \xi = \frac{X - X_c - c_0 t}{L}, \quad X_c = \frac{L}{4}. \tag{29}$$

Using Eq. (29), an explicit travelling-wave solution is

$$\begin{aligned} u(X,t) &= \frac{aL}{2\pi S}\sum_{m=1}^{8}\frac{w_m}{m}\sin(2\pi m\xi), \\ e(X,t) &= F - 1 = \frac{a}{S}\sum_{m=1}^{8} w_m \cos(2\pi m\xi), \\ v(X,t) &= V - c_0 e(X,t), \qquad P(X,t) = Ee(X,t). \end{aligned} \tag{30}$$

The wave-amplitude is $a = 0.20$, giving $0.8 \leq F \leq 1.2$. Initial particle states are sampled from the analytical solution at $t = 0$. Periodic reduction is used only for UL support lookup; particle trajectories and position errors retain unwrapped coordinates.

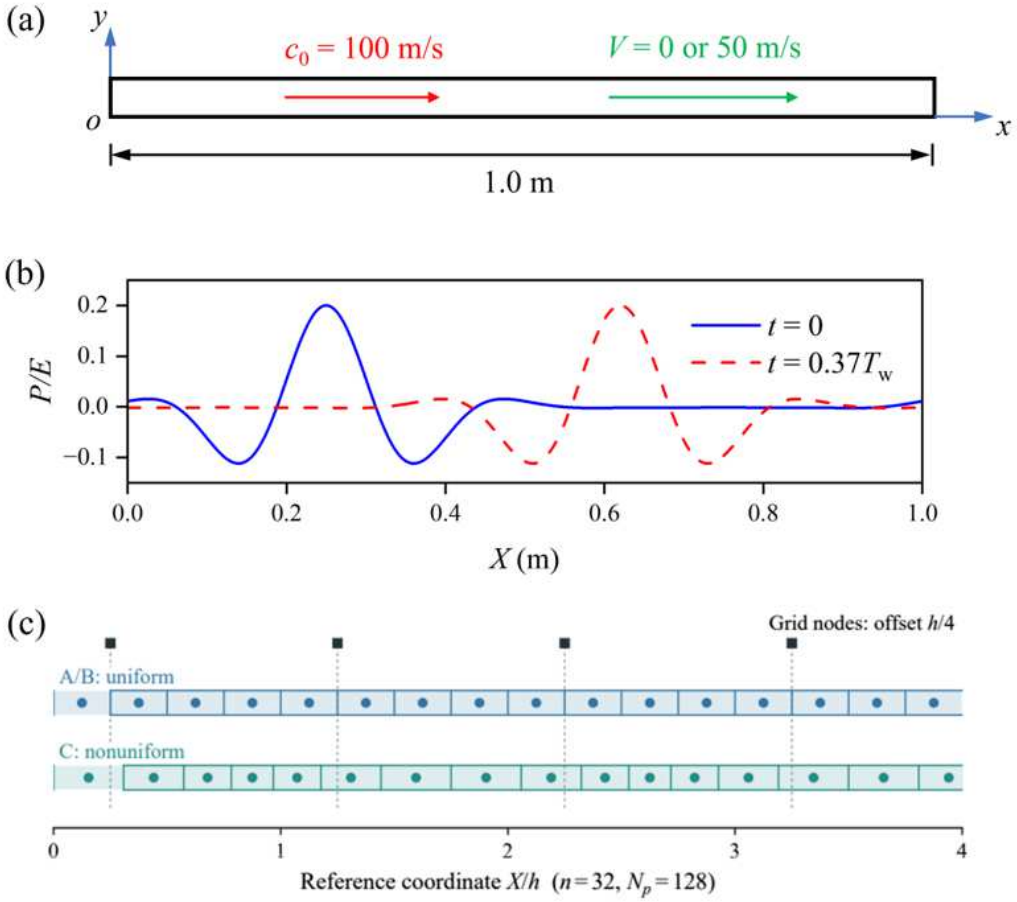


Figure 4: Multiharmonic travelling-wave benchmark: (a) periodic elastic medium; (b) analytical strain profiles; (c) uniform and nonuniform reference particle distributions.

The four schemes are TLMPM, TLBSMPM, ULMPM and ULBSMPM. They use the same double-precision Fortran MUSL kernel, lumped mass, constitutive law and time schedule. TLMPM and ULMPM use linear interpolation; TLBSMPM and ULBSMPM use cubic B-splines. The total Lagrangian methods cache reference support, basis gradients and nodal masses, whereas the updated Lagrangian meth-

ods update current support and nodal masses at each step. For this one-dimensional model, $\sigma = P$ and $N_{,X} = FN_{,x}$ relate the spatial and material force integrals. No artificial viscosity, stress smoothing, filtering or method-specific correction is introduced.

Table 1 defines three groups at $n = 32, 64, 128, 256, 512$ cells, with $h = L/n$, mean particle count $N_p/n = 4$, grid-origin offset $h/4$ and end time $5T_{\mathrm{w}} = 0.05$ s. Group B changes only the uniform drift relative to A; group C changes only the reference particle quadrature, as shown in Figure 4(c). For C, let $d = L/N_p$, $b_0 = 0$ and $b_{N_p} = L$, with internal partition boundaries

$$\begin{aligned} b_j &= jd + 0.30d\sin(2\pi j/7), \qquad 1 \le j < N_p, \\ X_p &= \tfrac{1}{2}(b_p + b_{p+1}), \qquad V_p^0 = b_{p+1} - b_p, \qquad m_p = \rho_0 V_p^0. \end{aligned} \tag{31}$$

Here $p = 0, \ldots, N_p - 1$, and the unit cross-sectional area is implicit in V_p^0. Equation (31) changes particle positions, volumes and masses consistently across methods. The prescribed perturbation is deterministic and is identical for all methods.

Table 1: Simulation groups for the multiharmonic travelling-wave benchmark.

Group	V/c_0	Particles	Comparison	Cases
A	0	Uniform	Accuracy baseline	20
B	0.5	Uniform	Uniform-drift sensitivity	20
C	0	Nonuniform	Particle-quadrature sensitivity	20
Total				60

The three main groups share the conservative time-step bound

$$\Delta t \le \frac{0.10h}{V_{\max} + (1 + 2a_{\max})c_0} = \frac{0.10h}{1.9c_0}, \qquad V_{\max} = 0.5c_0, \quad a_{\max} = 0.20. \tag{32}$$

All groups share the step bound of Eq. (32). Identical step sequences end exactly at 401 equally spaced primary observation times in $[0, 5T_{\mathrm{w}}]$ and at the additional snapshots $0.37T_{\mathrm{w}}$, $1.13T_{\mathrm{w}}$ and $2.41T_{\mathrm{w}}$. The implementation divides each interval between consecutive observation times into equal substeps satisfying the bound.

Errors compare each particle with the analytical state at its own material label. For a residual r_p, define a reference-volume-weighted norm and a fixed continuous

stress scale:

$$\|r\|_0 = \left(\frac{1}{L}\sum_p V_p^0 r_p^2\right)^{1/2}, \quad P_{\mathrm{rms}} = \frac{Ea}{S}\left(\frac{1}{2}\sum_{m=1}^{8} w_m^2\right)^{1/2},$$
$$\varepsilon_P(t) = \frac{\|P^{\mathrm{num}} - P^{\mathrm{exact}}\|_0}{P_{\mathrm{rms}}}, \quad \varepsilon_P^{\max} = \max_{t\in\mathcal{T}_{401}} \varepsilon_P(t). \tag{33}$$

The primary metric in Eq. (33) is the maximum over the prescribed sampling set $\mathcal{T}_{401}$. Unlike Eq. (21), it uses particle-volume weights and a fixed continuous analytical scale, making the denominator independent of particle quadrature. Additional measures include velocity and unwrapped-position errors, maximum pointwise stress error, harmonic amplitude and phase, total momentum, and the drift-subtracted energy

$$\mathcal{H}_h(t) = \sum_p V_p^0 \left[\frac{\rho_0}{2}(v_p - V)^2 + \frac{E}{2}(F_p - 1)^2\right]. \tag{34}$$

Changes in Eq. (34) are measured relative to its initial discrete value, with the initial integration error reported separately. Nonuniform-particle harmonic diagnostics use volume-weighted least squares.

All methods were timed using the same serial double-precision `gfortran -O3` build. For each main configuration, five runs were performed after warm-up. Total wall-clock time includes initialisation and time stepping and is the primary cost measure. Table 3 reports the median and range of the five timing runs.

Figure 5 and Table 2 report the complete main stress-error matrix. Velocity and unwrapped-position errors use the same norm and sampling set, with fixed denominators $v_{\mathrm{rms}} = c_0 P_{\mathrm{rms}}/E$ and $u_{\mathrm{rms}} = aL(2\pi S)^{-1}[\frac{1}{2}\sum_m (w_m/m)^2]^{1/2}$. No drift contribution is included in these denominators.

With uniform particles, TLMPM is more accurate than TLBSMPM at every tested resolution. At $n = 512$, both A and B give $\varepsilon_P^{\max} = 0.06279$ for TLMPM and 0.15175 for TLBSMPM. ULBSMPM gives approximately 0.15107, close to but slightly below the TLBSMPM error. Increasing the interpolation degree alone does not improve travelling-wave accuracy in this MUSL implementation. Groups A and B differ only in uniform drift, so their comparison isolates its effect. At $n = 512$, drift leaves the stress errors of TLMPM, TLBSMPM and ULBSMPM unchanged. The ULMPM error increases from 1.22811 in A to 3.18585 in B. Drift sensitivity therefore differs substantially among the methods in this benchmark.

The error ordering changes for nonuniform particles on the finer grids. At $n = 512$ in C, the stress errors are 0.74091, 0.15497, 1.32912 and 0.22807 for TLMPM,

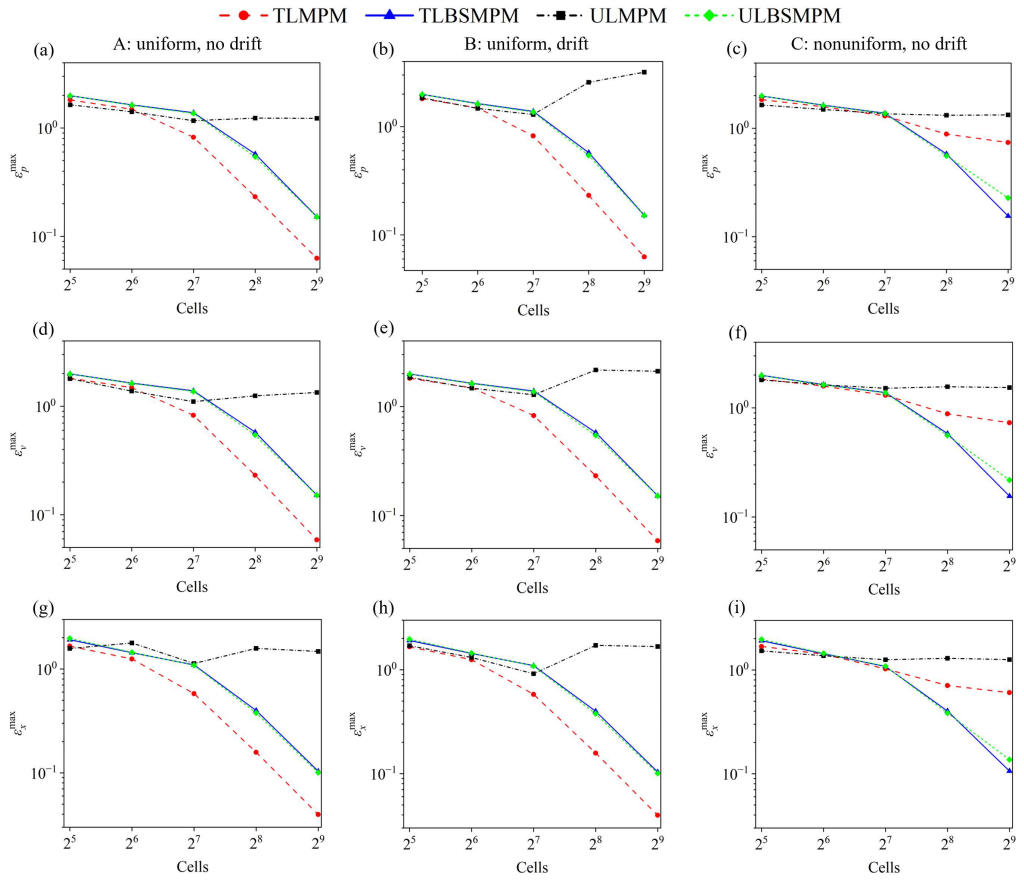


Figure 5: Sampled maximum normalised stress, velocity and unwrapped-position errors versus grid resolution for travelling-wave groups A, B and C.

Table 2: Dimensionless sampled maximum stress errors $\varepsilon_P^{\max}$ for the four methods at different travelling-wave grid resolutions.

Group	n	TLMPM	TLBSMPM	ULMPM	ULBSMPM
A	32	1.81405	1.98898	1.63754	1.98449
A	64	1.48943	1.63294	1.41038	1.62191
A	128	0.82154	1.38530	1.16844	1.36558
A	256	0.23220	0.57538	1.23360	0.54277
A	512	0.06279	0.15175	1.22811	0.15107
B	32	1.81405	1.98898	1.84608	1.98435
B	64	1.48943	1.63294	1.47420	1.62190
B	128	0.82154	1.38530	1.29615	1.36557
B	256	0.23220	0.57538	2.56967	0.54277
B	512	0.06279	0.15175	3.18585	0.15107
C	32	1.83883	1.98886	1.64055	1.98391
C	64	1.58023	1.63272	1.49264	1.62180
C	128	1.29861	1.37655	1.36148	1.36785
C	256	0.88447	0.57913	1.31964	0.55679
C	512	0.74091	0.15497	1.32912	0.22807

TLBSMPM, ULMPM and ULBSMPM, respectively. TLBSMPM reduces this error by 79.1% relative to TLMPM and 32.1% relative to ULBSMPM. The ratios of the C-group to A-group stress errors are 1.021, 11.80, 1.082 and 1.510 for TLBSMPM, TLMPM, ULMPM and ULBSMPM, respectively. Although the ULMPM ratio is close to unity, its normalised stress errors remain high in both groups. TLBSMPM has the lowest error in group C and limited sensitivity to the prescribed quadrature perturbation. Velocity and position errors show the same ordering on the finest grid (Table 3). However, the maximum normalised stress error remains 15.5% at $n = 512$. These results support improved robustness to the specified quadrature perturbation, with accuracy still limited by the reported error. They do not establish robustness for arbitrary nonuniform particle arrangements.

Table 3: Normalised stress, velocity and position errors and total wall-clock times for the travelling-wave benchmark at $n = 512$.

Group	Method	$\varepsilon_P^{\max}$	$\varepsilon_v^{\max}$	$\varepsilon_x^{\max}$	Median (s)	Range (s)
A	TLMPM	0.06279	0.05884	0.03972	2.062	1.568–2.107
A	TLBSMPM	0.15175	0.15182	0.10358	3.070	3.002–3.125
A	ULMPM	1.22811	1.33956	1.47564	3.379	3.182–3.779
A	ULBSMPM	0.15107	0.15112	0.10071	6.310	6.193–6.389
B	TLMPM	0.06279	0.05884	0.03972	1.656	1.551–1.885
B	TLBSMPM	0.15175	0.15182	0.10358	3.079	2.311–3.156
B	ULMPM	3.18585	2.10859	1.67065	3.779	3.691–4.268
B	ULBSMPM	0.15107	0.15112	0.10071	6.683	6.509–6.772
C	TLMPM	0.74091	0.73110	0.60460	1.725	1.539–2.065
C	TLBSMPM	0.15497	0.15495	0.10599	3.054	3.008–3.071
C	ULMPM	1.32912	1.53442	1.25609	3.419	3.195–3.687
C	ULBSMPM	0.22807	0.21820	0.13659	6.311	6.138–6.359

The local refinement slope $p_{256:512} = \log_2[\varepsilon_P^{\max}(256)/\varepsilon_P^{\max}(512)]$ is 1.923 for TLBSMPM in A/B and 1.902 in C. TLMPM gives 1.887 in A/B but only 0.256 in C; ULBSMPM gives 1.845 in A/B and 1.288 in C. ULMPM shows no consistent error reduction, including a slope of −0.310 in B. These observed slopes combine spatial, temporal and transfer errors over one refinement interval. They do not establish the spatial convergence order of the methods. The fixed mean particle count and changing nonuniform quadrature prevent isolation of a single discretisation error.

Figure 6 compares unprocessed stress profiles with the exact travelling wave at the three prescribed noninteger transit times. Figure 7 shows the final pointwise residual and the full primary stress-error history. ULMPM develops strong fluctua-

tions at the particle scale, particularly in the drifting case. TLMPM reproduces the smooth waveform more accurately for uniform particles, but its accuracy decreases under nonuniform quadrature. The cubic interpolation methods reduce stress fluctuations at the particle scale. The profiles are neither smoothed nor shifted to align their phase with the reference.

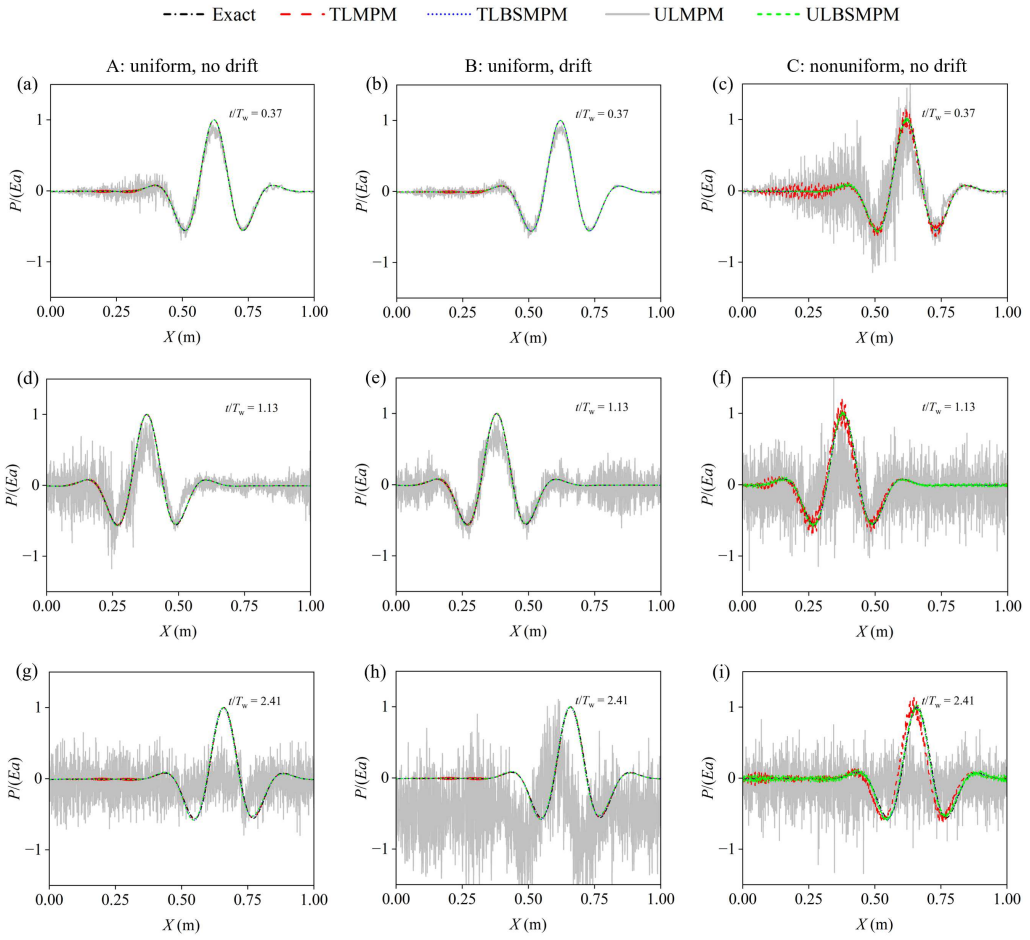


Figure 6: Numerical and analytical stress profiles for travelling-wave groups A, B and C at $t/T_w = 0.37$, 1.13 and 2.41.

3.2. Pure bending of an elastic beam

The pure-bending benchmark assesses stress accuracy, convergence behaviour and computational cost in a two-dimensional linear-elastic beam. The model is

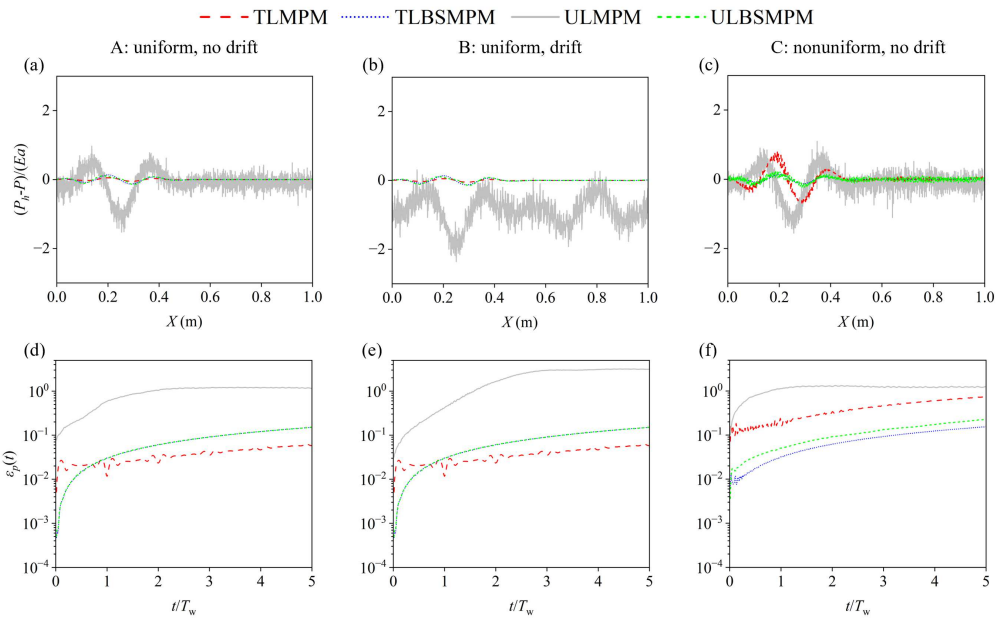


Figure 7: Travelling-wave stress errors on the finest grid: final pointwise residuals (top) and volume-weighted error histories (bottom).

shown in Figure 8. The beam has a length of $L = 1.2$ m and a height of $d = 0.1$ m. The pin and roller supports are located a distance $a = 0.1$ m from the left and right ends of the beam, respectively. Equal downward concentrated forces, each with magnitude $F(t)$, are applied at the two overhanging ends. The load is increased linearly according to

$$F(t) = F_{\max}\frac{t}{t_f}, \qquad 0 \le t \le t_f, \tag{35}$$

where $F_{\max} = 250\,\mathrm{N}$ and $t_f = 5\,\mathrm{s}$. Consequently, the bending moment in the segment between the two supports is spatially constant and given by

$$M(t) = aF(t), \tag{36}$$

where $a = 0.1$ m is the distance between either support and the corresponding overhanging end. Thus, $M(t_f) = 25\,\mathrm{N\,m}$. The Young's modulus is $E = 10\,\mathrm{MPa}$, the Poisson's ratio is $\nu = 0.2$, and the density is $\rho = 1000\,\mathrm{kg\,m^{-3}}$. The beam segment between the supports is subjected to pure bending.

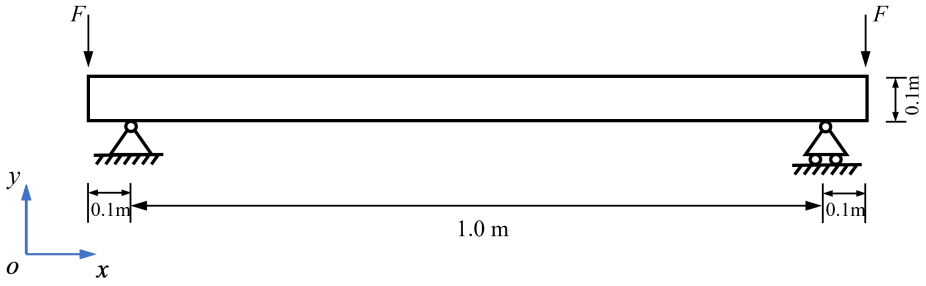


Figure 8: Geometry and loading of the elastic beam under pure bending.

At the final loading time $t_f = 5\,\mathrm{s}$, the response is assumed to be in quasi-static equilibrium. The analytical axial stress in the pure-bending segment is therefore

$$\sigma_{xx}(y, t_f) = \frac{M(t_f)\,(y - y_{\mathrm{NA}})}{I}, \tag{37}$$

where $y_{\mathrm{NA}} = 0.05$ m is the neutral-axis position measured from the bottom surface, $M(t_f) = 25\,\mathrm{N\,m}$ is the final bending moment, and I is the second moment of area. For unit out-of-plane thickness, $b = 1$ m, and the second moment of area is

$$I = \frac{bd^3}{12} = 8.33 \times 10^{-5}\,\mathrm{m}^4. \tag{38}$$

Figure 9 compares the axial stress σ_{xx} predicted by the four methods. Panel a shows contours at $t = 5\,\mathrm{s}$ in the segment $0.6 \le x \le 0.8\,\mathrm{m}$. ULMPM produces pronounced spatial oscillations, whereas TLMPM, TLBSMPM and ULBSMPM produce smoother stress fields. Panel b compares stress profiles along the sampled horizontal particle row for $\Delta x = 0.0025\,\mathrm{m}$. Both updated Lagrangian methods show oscillations, while TLMPM and TLBSMPM are closer to the analytical profile. The enlarged view shows closer agreement for TLBSMPM than for TLMPM. In this bending case, total Lagrangian transfer reduces stress oscillations, and B-spline interpolation further reduces error relative to TLMPM.

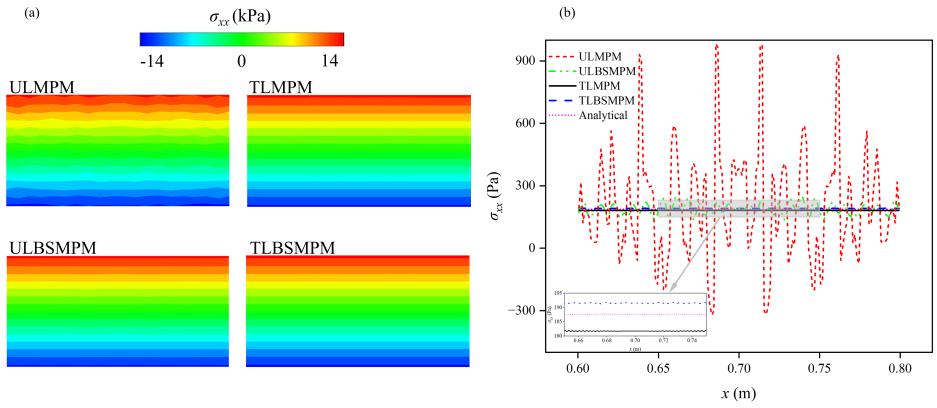


Figure 9: Axial stress σ_{xx} in the pure-bending beam: (a) stress contours; (b) numerical and analytical stress profiles.

Stress accuracy is measured by the relative discrete L_2 error of Eq. (21), with $u_p = \sigma_{xx,p}$. The sampling set $\mathcal{S}$ contains particles in $0.6 \le x_p \le 0.8\,\mathrm{m}$, reducing local effects from the supports and concentrated forces. Numerical and analytical axial stresses are compared at the same material-point locations.

Figure 10a shows the relative axial-stress L_2 errors for the four methods at $t = 5\,\mathrm{s}$ and different grid sizes. For the tested grids, TLMPM has lower errors than ULMPM, and TLBSMPM has lower errors than ULBSMPM. Comparing TLMPM with TLBSMPM quantifies the effect of replacing linear interpolation with B-spline interpolation within the total Lagrangian framework.

Figure 10b compares total CPU time with the relative axial-stress L_2 error for the four methods at different grid sizes and CFL numbers. The serial Fortran 90 program runs on a 64-bit Linux workstation with two Intel Xeon Scalable Gold 5218 CPUs and 128 GB of RAM. CPU time is measured with the intrinsic `CPU_TIME` subroutine, whereas the wave benchmark reports wall-clock time. At

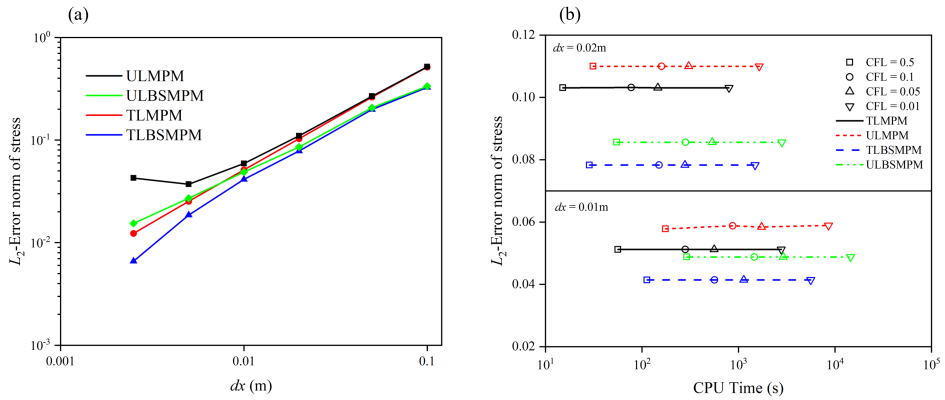


Figure 10: Pure-bending benchmark: (a) relative axial-stress L_2 error versus grid size; (b) total CPU time versus error for different Courant–Friedrichs–Lewy (CFL) numbers.

the same grid size, the updated Lagrangian methods require more CPU time than their total Lagrangian counterparts. Reference support caching avoids repeated evaluation of basis functions and gradients. The larger B-spline support still contributes to particle–grid transfer cost at every time step.

3.3. Heat conduction in a square slab

The two-dimensional homogeneous square slab used to test heat conduction is shown in Figure 11. The computational domain is defined by $0 \le x \le L$ and $0 \le y \le H$, where $L = H = 1.5$ m. The initial temperature is uniform:

$$T(x, y, 0) = T_0 = 0\,^{\circ}\mathrm{C}. \tag{39}$$

For $t > 0$, a constant temperature of $T_1 = 100\,^{\circ}\mathrm{C}$ is prescribed on all four boundaries:

$$T(0, y, t) = T(L, y, t) = T(x, 0, t) = T(x, H, t) = T_1 \tag{40}$$

Under these initial and boundary conditions, the analytical temperature distribution is given by

$$T(x, y, t) = T_1 + \frac{16(T_0 - T_1)}{\pi^2} \sum_{i=1,3,\ldots}^{\infty} \sum_{j=1,3,\ldots}^{\infty} \frac{\exp\left[-k_d \pi^2 \left(\frac{i^2}{L^2} + \frac{j^2}{H^2}\right) t\right]}{ij} \sin\left(\frac{i\pi x}{L}\right) \sin\left(\frac{j\pi y}{H}\right). \tag{41}$$

The thermal diffusivity is $\alpha = k/(\rho c)$, where k, ρ and c denote thermal conductivity, density and specific heat capacity, respectively. In Eq. (41), k_d denotes this diffusivity ($k_d = \alpha$). To resolve the transient within the selected simulation time, the conductivity is set to $k = 20{,}000\,\mathrm{W\,m^{-1}\,K^{-1}}$. This is 5000 times the reference value of $4\,\mathrm{W\,m^{-1}\,K^{-1}}$. The increased conductivity accelerates the thermal transient and does not represent a typical concrete property. The density is $\rho = 2600\,\mathrm{kg\,m^{-3}}$, and the specific heat capacity is $c = 900\,\mathrm{J\,kg^{-1}\,K^{-1}}$.

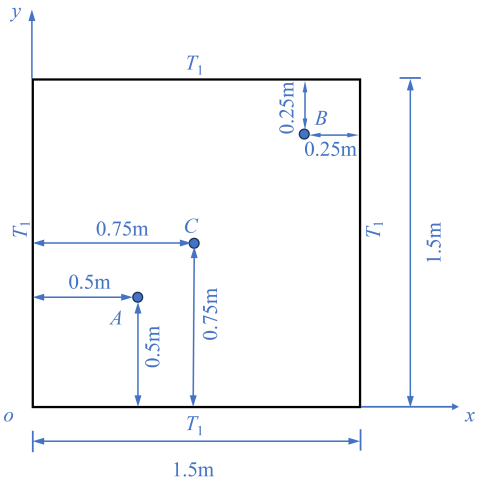


Figure 11: Geometry and prescribed boundary temperatures of the square slab.

For the TLBSMPM analysis, the grid spacing is 0.03 m. Four material points are placed in each background cell in a 2×2 arrangement. The time step is $\Delta t = 1.0 \times 10^{-5}$ s, and the total simulation time is 60 s.

Figure 12a shows temperature contours at $t = 5$, 10, 20, and 30 s. All four boundaries are maintained at 100°C, so heat diffuses inward towards the centre. The central low-temperature region contracts, and the temperature field becomes more uniform with time.

Figure 12b presents the pointwise relative-error contours between the numerical and analytical temperatures at the corresponding material-point locations. The pointwise relative error at material point p is defined as

$$e_p^{\mathrm{rel}}(t) = \frac{\left|T_p^{\mathrm{num}}(t) - T_p^{\mathrm{ana}}(t)\right|}{\left|T_p^{\mathrm{ana}}(t)\right|}. \tag{42}$$

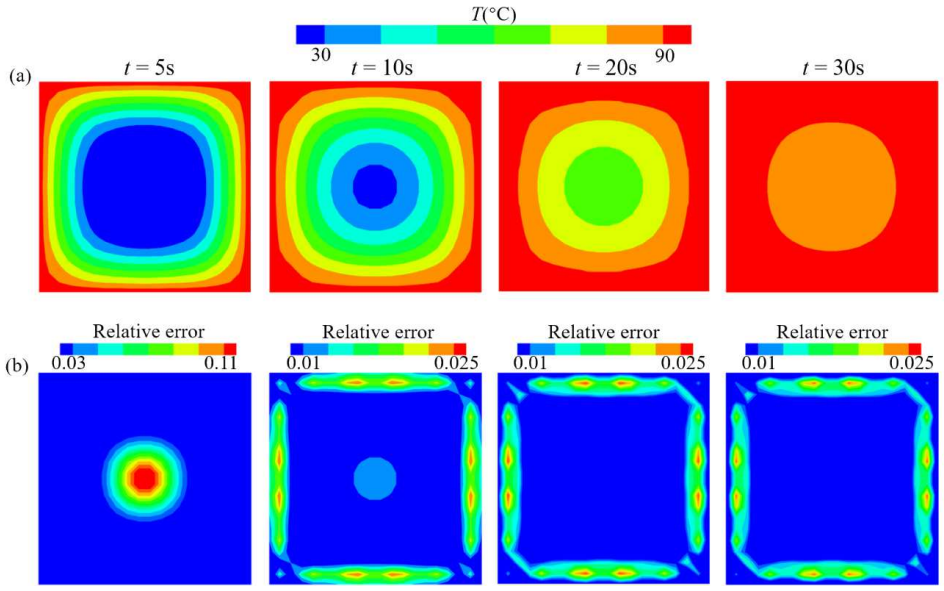


Figure 12: Square-slab heat conduction: (a) temperature contours; (b) pointwise relative-temperature-error contours.

Here, T_p^{num} and T_p^{ana} denote the numerical and analytical temperatures at material point p, respectively. The small pointwise relative errors at the four selected times indicate agreement between TLBSMPM and the analytical solution. At $t =$ 5 s, the largest relative errors occur near the slab centre. The analytical temperature remains close to its initial value in this region. Normalisation by this small temperature can amplify the relative error.

As the centre temperature rises, the relative error decreases in the interior and becomes concentrated near the boundaries. Material points within one grid spacing of each boundary are assigned a temperature of 100°C. These points do not coincide with the mathematical boundaries, which introduces a boundary discretisation error. Their analytical temperatures are approximately 96.0°C, 97.5°C, 98.9°C, and 99.5°C at $t = 5$, 10, 20, and 30 s, respectively. The difference between prescribed and analytical temperatures produces relative-error peaks near all four boundaries.

Temperature-field accuracy is measured by the relative discrete L_2 error of Eq. (21), with $u_p = T_p$. The sampling set $\mathcal{S}$ contains particles satisfying $0.2 \le x_p \le 1.3$ m and $0.2 \le y_p \le 1.3$ m. This interior-domain measure reduces the influence of the prescribed-temperature boundary strips. Unlike the pointwise error of Eq. (42),

it normalises the summed squared residuals by the summed squared analytical temperatures.

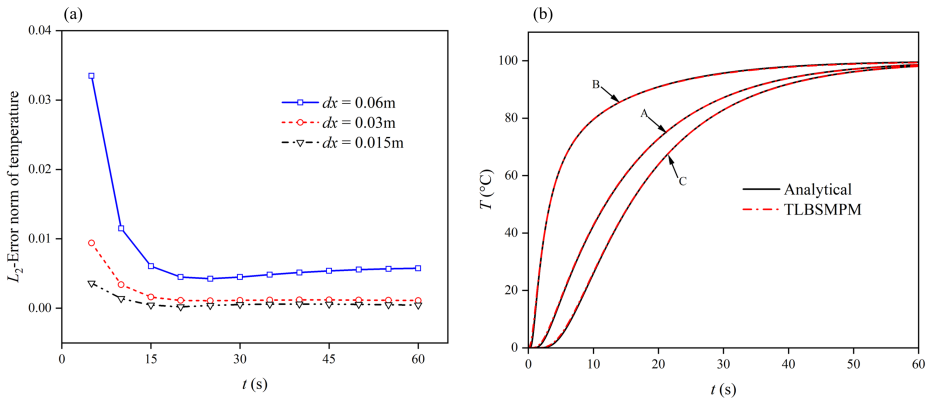


Figure 13: Square-slab heat conduction: (a) interior-domain relative L_2 error histories; (b) numerical and analytical temperature histories at points A, B and C.

Figure 13a shows the interior-domain relative L_2 error for different grid sizes. The error decreases with grid refinement. Initially, the sudden boundary heating produces steep temperature gradients that are less well resolved on coarse grids. As heat diffuses inward and the field becomes smoother, the relative L_2 error decreases before approaching a nearly steady level. Figure 13b compares temperature histories at points A, B and C with the analytical solution.

3.4. Cantilever beam vibration under thermal shock

The two-dimensional homogeneous thermoelastic cantilever beam is shown in Figure 14. The beam has a length of $L = 0.5$ m and a height of $H = 0.05$ m, and its left end is fully fixed. The initial temperature is uniform at $T = 20°\text{C}$. At $t = 0$, a thermal shock is applied by prescribing $T_{\text{upper}} = 20°\text{C}$ and $T_{\text{lower}} = 200°\text{C}$ on the upper and lower surfaces, respectively. These temperatures are maintained during the subsequent simulation. The Young's modulus and density of the beam are $E = 50.0$ GPa and $\rho = 2600\,\text{kg/m}^3$, respectively. The background-grid spacing is $\Delta x = 0.0025$ m, the time step is $\Delta t = 1.0 \times 10^{-7}$ s, and four material points are placed in each background cell in a 2×2 arrangement.

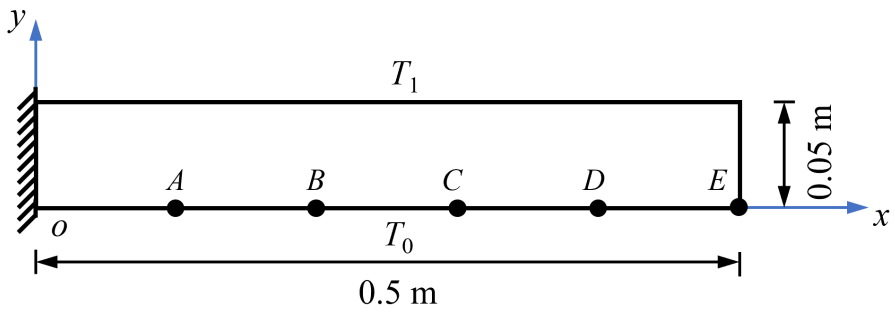


Figure 14: Geometry and thermal loading of the thermoelastic cantilever beam.

For a uniform Euler–Bernoulli cantilever beam, the first natural frequency predicted by classical beam theory is

$$f_1 = \frac{\beta_1^2}{2\pi L^2}\sqrt{\frac{EI}{\rho A}}, \tag{43}$$

where $\beta_1 = 1.875$ is the first dimensionless modal root, A is the cross-sectional area, and I is the second moment of area. For unit out-of-plane thickness, $b = 1\,\mathrm{m}$, the beam-theory frequency is $f_1 = 141.7\,\mathrm{Hz}$. Figure 15 shows the normalised displacement signal and its frequency spectrum from TLBSMPM. The extracted dominant frequency is 142.76 Hz, approximately 0.75% above the beam-theory estimate.

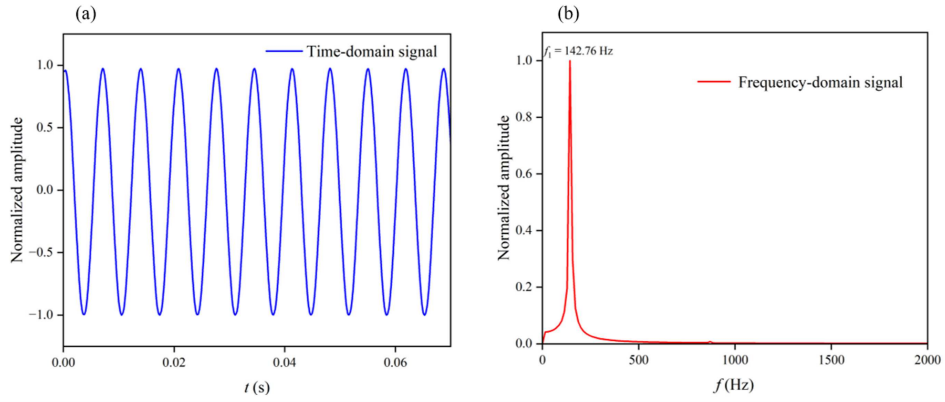


Figure 15: Cantilever response under thermal shock: (a) normalised displacement history; (b) frequency spectrum.

The numerical dominant frequency agrees closely with the fundamental bending frequency predicted by beam theory. Young's modulus and density are temperature independent, and the frequency reference uses the undeformed beam geometry. The imposed temperature difference drives transient thermal deformation and stress without temperature-dependent stiffness degradation.

Figure 16 shows the cantilever's vertical displacement, magnified by a factor of 10,000 for visualisation. In Figure 16a, the nonuniform temperature field induces differential thermal expansion through the beam depth. The resulting thermal curvature causes downward deflection under the fixed-end constraint. Displacement magnitude increases towards the free end, while transverse displacement remains zero at the fixed end. Figure 16b shows vertical-displacement histories at points A–E, located at $x = 0.1$, 0.2, 0.3, 0.4 and 0.5 m, respectively. The oscillations are consistent with the approximately 140 Hz first natural frequency obtained from TLBSMPM.

3.5. Impact loading of a concrete disk

This example investigates a two-dimensional thick-walled concrete disk subjected to an internal pressure pulse. Homogeneous and three-phase concrete models are compared in terms of temperature evolution, stress-wave propagation and damage development. The model is shown in Figure 17a. The inner and outer diameters are $d = 50$ mm and $D = 152$ mm, respectively. The applied pressure is $P(t) = P_0 \exp\left[-\left((t - 2t_f)/t_f\right)^2\right]$, where $t_f = 0.0025$ s. This Gaussian pulse reaches

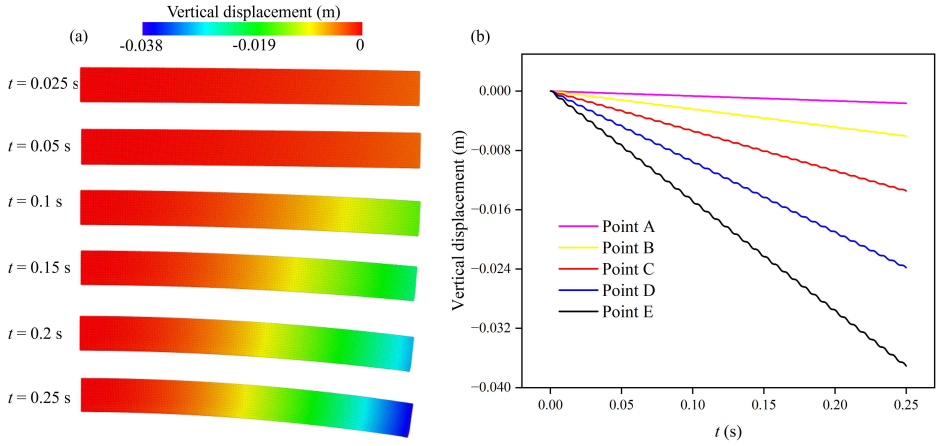


Figure 16: Vertical displacement of the thermally shocked cantilever: (a) displacement contours; (b) displacement histories at points A–E.

its peak $P_0 = 400\,\text{MPa}$ at $t = 2t_f = 5\,\text{ms}$ and decays to a negligible value by approximately 10 ms, consistent with Figure 17b.

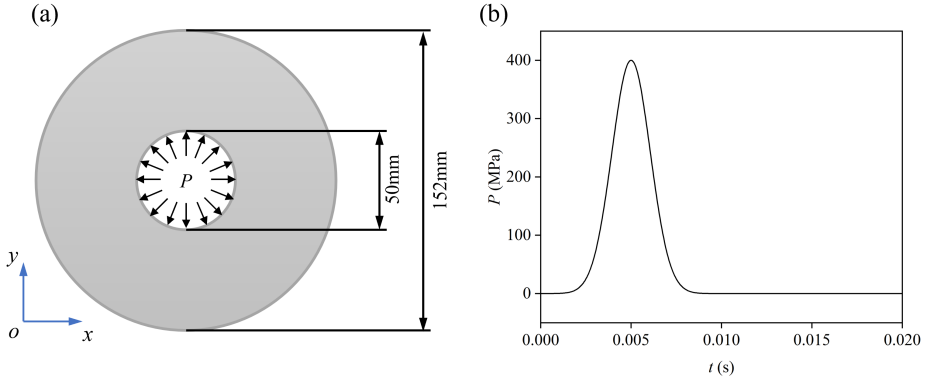


Figure 17: Thick-walled concrete disk: (a) geometry and internal pressure loading; (b) pressure-pulse history.

Figure 18 shows the five concrete models used to examine material heterogeneity and aggregate area fraction. They comprise one homogeneous model and four three-phase models with aggregate area fractions of 23.3%, 31.5%, 38.8% and 46.6%. Each three-phase model consists of mortar, coarse aggregates and ITZs, shown in blue, green and red, respectively. The 23.3% model serves as

the heterogeneous baseline, and higher area fractions are obtained by adding aggregates.

The Young's moduli of mortar, aggregates and ITZ are 20.0, 45.0 and 16.0 GPa, respectively. Their corresponding densities are 2600, 2700 and 2200 kg/m^3. The background-grid spacing is 1 mm, and the time step is $\Delta t = 1.0 \times 10^{-6}$ s.

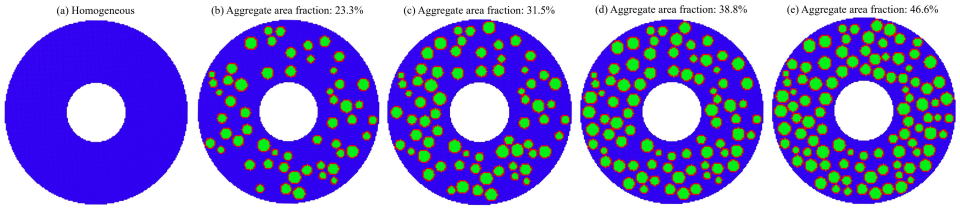


Figure 18: Concrete-disk models with aggregate area fractions of (a) 0% (homogeneous concrete), (b) 23.3%, (c) 31.5%, (d) 38.8% and (e) 46.6%.

Figure 19a compares temperatures in the five concrete models at t = 5, 7, 25, 45 and 87 ms. At peak pressure (t = 5 ms), the plotted scale shows no appreciable temperature rise. During the descending portion of the pulse, localised heating appears near the inner surface at t = 7 ms. This rise is consistent with the conversion of inelastic work into heat in the model.

The three-phase models show more heterogeneous temperature fields than the homogeneous model, with temperature rises concentrated in and around the ITZs. The lower ITZ stiffness and strength favour local inelastic deformation and damage. Aggregate temperature variations remain relatively small, although phase-dependent conductivity, heat capacity and inelastic dissipation can affect the temperature contrast. Heated regions extend outward similarly in the four three-phase models, but local temperature distributions differ. For these generated mesostructures, higher aggregate area fractions are associated with more fragmented temperature contours near the inner wall. The observed differences primarily concern local temperature heterogeneity, without a uniform shift in overall temperature.

Figure 19b compares equivalent-stress contours in the five concrete models at the same five times. The homogeneous model shows smoother and more nearly axisymmetric stress-wave propagation than the three-phase models. In the three-phase models, contrasts between mortar, aggregate and ITZ properties cause wave reflection, transmission and scattering at phase interfaces. The equivalent-stress field is less uniform and contains more local spatial variations. High stresses develop in or near stiff aggregates and phase interfaces through local load transfer

and wave interactions. In the four three-phase models, relatively high equivalent stresses are concentrated near the inner wall at $t = 7$ ms. This annular pattern is similar across aggregate area fractions, but local stress distributions differ. The 46.6% model shows finer and more closely spaced local stress variations than the 23.3% model. At $t = 25$, 45, and 87 ms, irregular stress variations extend over more of the disk wall. The locations, shapes and connectivity of high-stress regions vary among the models. These differences are consistent with stress-wave interactions and local load transfer associated with aggregate arrangements and phase interfaces.

Figure 19c compares damage in the five concrete models at the same times. In the three-phase models, damage is concentrated in and around the ITZs. Aggregate damage remains zero because the aggregate constitutive law excludes damage evolution. At $t = 5$ ms, no damage is visible at the plotted scale. At $t = 7$ ms, damage is concentrated in a narrow, approximately annular region next to the inner surface.

As damage extends outward, its spatial distribution increasingly differs among the models. The homogeneous model shows a more continuous, nearly axisymmetric pattern, whereas the three-phase models show fragmented and irregular regions. At $t = 45$ and 87 ms, the 23.3% model has relatively continuous damaged patches near the inner wall. The 31.5% model shows a more segmented distribution, while the 38.8% and 46.6% models show network-like and locally ring-shaped patterns. These differences suggest that aggregate arrangement and phase interfaces influence damage localisation and spatial connectivity.

Figure 20 reports the mass-weighted global damage D_{global} defined in Eq. (22). Since particle masses are constant, its rate is

$$\frac{\mathrm{d}D_{\mathrm{global}}}{\mathrm{d}t} = \frac{\sum_p m_p \dot{D}_p(t)}{\sum_p m_p}. \tag{44}$$

Aggregate particles carry $D_p = 0$ while their mass remains in the denominator. Equation (23) therefore bounds D_{global} by $1 - w_{\mathrm{a}}$ when mortar and ITZ damage remain within $[0, 1]$. Aggregate area fraction describes the geometry, whereas w_{a} is the mass fraction; they differ when phase densities differ.

Figure 20 shows five stages of global damage accumulation, with the ordering of the four models changing over time. The curve slopes represent the mass-weighted damage accumulation rate defined in Eq. (44). During stage I (0–5 ms),

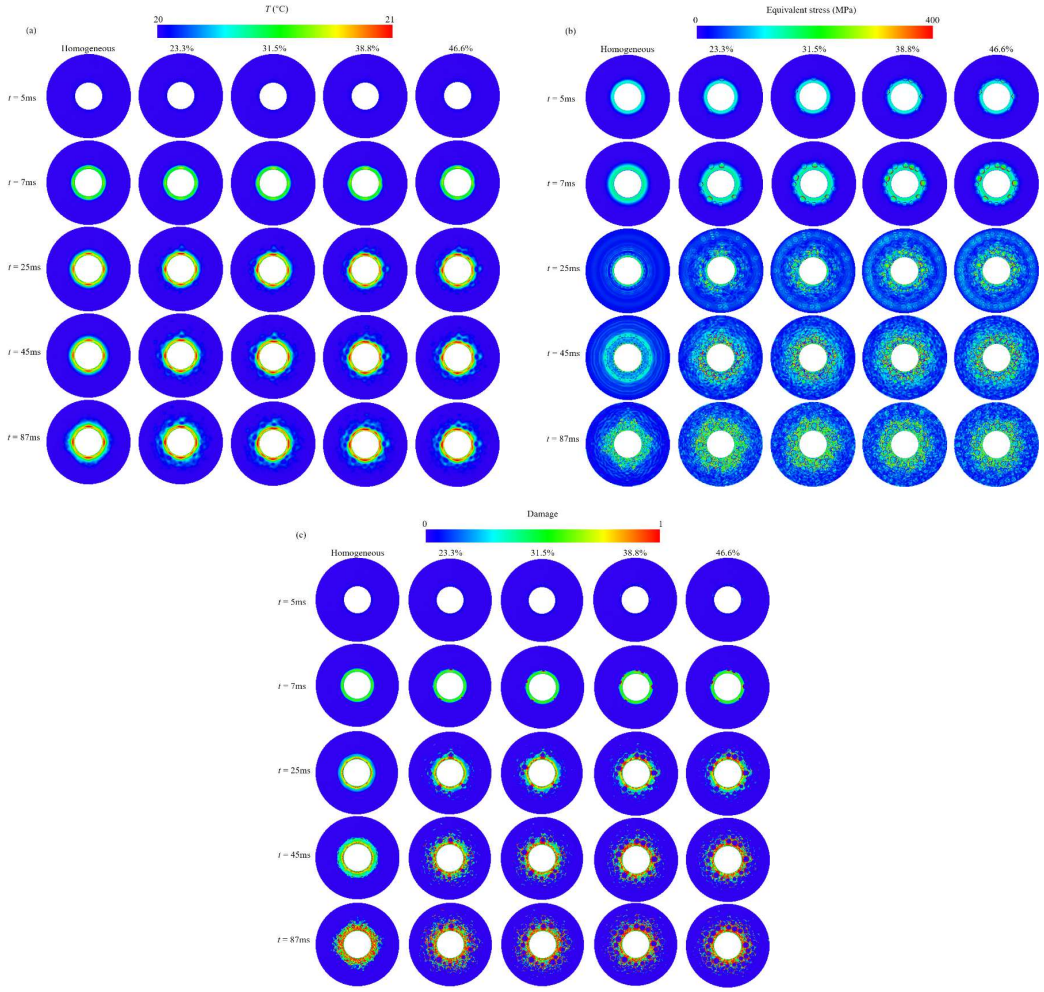


Figure 19: Contours in homogeneous and three-phase concrete disks at selected times: (a) temperature; (b) equivalent stress; (c) damage.

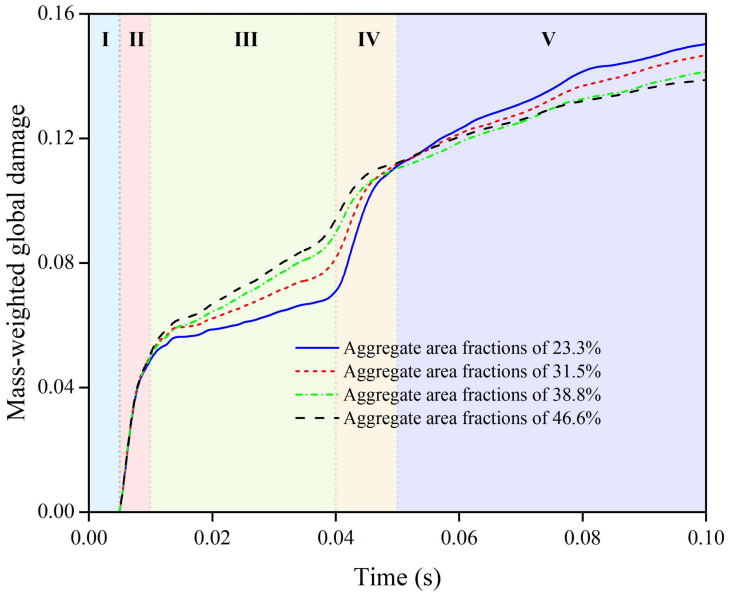


Figure 20: Mass-weighted global damage histories for concrete disks with different aggregate area fractions and five marked stages.

global damage remains negligible at the plotted scale as the pressure pulse rises. Stage II (5–10 ms) shows a rapid, nonlinear increase during the descending portion of the pulse, with the four histories remaining close. During stage III (10–40 ms), damage accumulates more slowly and the curves progressively separate. Higher aggregate area fractions generally correspond to greater global damage later in this interval. Stage IV (40–50 ms) shows a second rapid increase, with larger damage increments in models with lower aggregate area fractions. These increments narrow the separation between the curves and begin to change their ordering.

During stage V (50–100 ms), damage accumulates at lower average rates, and successive curve crossings establish the reverse ordering by approximately 75 ms. At 100 ms, D_{global} is approximately 0.1503, 0.1468, 0.1415 and 0.1388 for aggregate area fractions of 23.3%, 31.5%, 38.8% and 46.6%, respectively. This late-stage ordering describes damage averaged over the total particle mass. Equation (23) combines the evolving mean damage in mortar and ITZ with a constant aggregate-mass weighting factor. The global histories do not establish whether higher aggregate content reduces damage in the damageable phases. They also cannot identify the mechanisms responsible for the second rapid rise.

4. Discussion

The benchmarks show that method performance depends on the problem and particle arrangement. In bending, the total Lagrangian formulations produce smaller spatial stress oscillations than the updated Lagrangian formulations (Figure 9). At 512 cells in the travelling-wave benchmark, TLBSMPM has a lower sampled maximum stress error for prescribed nonuniform quadrature (0.15497 versus 0.74091). Uniform particles favour TLMPM, with a stress error of 0.06279 versus 0.15175 for TLBSMPM. Slab temperature errors decrease with grid refinement, and the cantilever's first natural frequency is 0.75% above the beam-theory estimate.

Reference support and basis continuity affect different aspects of the mechanical calculation. Fixed-reference support avoids repeated evaluation of basis functions and nodal masses. The continuity of the cubic basis may reduce numerical stress fluctuations at the particle scale. All methods use the same particle set within each configuration, and separate configurations test drift and particle quadrature. Modified gradients and interpolation change spatial differentiation [42, 43], whereas dual-domain, subdomain and dual-interface methods change particle integration [44–46]. Staggered grids and cell-based integration modify other components of the discrete balance [47–49]. Comparisons with MPM–SPH require matching the physical mechanisms and response measures [50].

The wave benchmark confirms that error ordering depends on particle distribution. With uniform particles at 512 cells, TLMPM has the lower stress error (0.06279 versus 0.15175). Prescribed nonuniform quadrature reverses this ordering and gives TLBSMPM the larger observed refinement slope over the final interval. These findings apply to the tested smooth wave and deterministic quadrature perturbation. They do not establish a general accuracy ranking for other particle arrangements or problems.

The disk example shows heterogeneous temperature and stress fields in the three-phase models, with damage localised in and around the ITZs. Global damage depends on damage evolution in mortar and ITZ and on the mass of undamaged aggregates included in the denominator. The stage-dependent ordering in Figure 20 applies to these generated mesostructures. It does not establish a general monotonic relationship between aggregate content and damage.

The examples evaluate the proposed phase-resolved formulation under elastic wave propagation, pure bending, fixed-geometry conduction, thermoelastic cantilever vibration and concrete-disk impact loading. The slab tests the heat-conduction calculation, and the cantilever compares the dominant vibration fre-

quency under thermal loading with beam theory. The disk tests heat transport with phase-specific constitutive response and damage evolution. These comparisons identify the effects of total Lagrangian transfer, basis choice and particle quadrature within the tested conditions. The disk results describe phase-resolved fields and distinguish local damage from the mass-weighted global measure.

5. Conclusion

This study developed TLBSMPM with fixed-reference cubic interpolation and a material-coordinate heat balance for thermomechanical analysis of concrete. Numerical benchmarks assessed accuracy, sensitivity to particle quadrature and computational cost.

At 512 cells, the prescribed nonuniform-particle wave gave sampled maximum stress errors of 0.15497 for TLBSMPM and 0.74091 for TLMPM. Uniform particles favoured TLMPM, with a stress error of 0.06279 versus 0.15175 for TLBSMPM. The TLBSMPM refinement slopes over the final refinement interval were 1.923 in the uniform groups and 1.902 in the nonuniform group. In bending, the total Lagrangian formulations reduced stress oscillations and required less computation time than the updated Lagrangian formulations at the same grid size. Slab temperature predictions approached the analytical solution as the grid was refined. The thermally shocked cantilever gave a fundamental frequency of 142.76 Hz, 0.75% above the beam-theory estimate. In the impact-loaded three-phase disk, damage was localised in and around the ITZs.

The formulation supports coupled thermomechanical calculations with distinct material properties for mortar, aggregates and ITZs. Its reported performance applies to the tested wave, bending, conduction, cantilever vibration and concrete-disk impact cases. Extensions to three-dimensional mesostructures and additional phase-specific constitutive models require further assessment.

CRediT authorship contribution statement

Haitao Ding: Writing - original draft, Investigation, Visualization. **Zheng Sun:** Writing - review and editing, Validation, Conceptualization, Funding acquisition. **Weiling Xiao:** Writing - review and editing, Validation. **Xiaomin Zhou:** Writing - review and editing, Supervision, Funding acquisition.

Declaration of competing interest

The authors declare that they have no known competing financial interests or personal relationships that could have appeared to influence the work described in this paper.

Acknowledgments

This work was funded by the National Natural Science Foundation of China (No. 12562021 and 12262013), and the Jiangxi Provincial Natural Science Foundation (No. 20262BAC240480 and 20262BAC240476).

Data Availability

Data will be made available on request.

References

[1] Q. Ma, R. Guo, Z. Zhao, Z. Lin, K. He, Mechanical properties of concrete at high temperature—A review, Construction and Building Materials 93 (2015) 371–383. 10.1016/j.conbuildmat.2015.05.131.

[2] T. Manzoor, J.A. Bhat, A.H. Shah, Performance of geopolymer concrete at elevated temperature – A critical review, Construction and Building Materials 420 (2024) 135578. 10.1016/j.conbuildmat.2024.135578.

[3] T. Zhang, H. Wu, H. Dong, Y. Lyu, X. Quan, F. Huang, Damage decoupled analysis of reinforced concrete slabs subjected to penetration and explosion: Experimental and numerical investigation, Engineering Failure Analysis 186 (2026) 110564. 10.1016/j.engfailanal.2026.110564.

[4] C. Gao, J. Yan, Y. Liu, F. Bai, Y. Xu, H. Zhu, W. Lu, F. Huang, Spalling damage on steel reinforced concrete structures under deep embedded explosion, Engineering Structures 343 (2025) 121093. 10.1016/j.engstruct.2025.121093.

[5] L. Li, V. Dao, P. Lura, Autogenous deformation and coefficient of thermal expansion of early-age concrete: Initial outcomes of a study using a newly-developed Temperature Stress Testing Machine, Cement and Concrete Composites 119 (2021) 103997. 10.1016/j.cemconcomp.2021.103997.

[6] M.R. Bangi, T. Horiguchi, Effect of fibre type and geometry on maximum pore pressures in fibre-reinforced high strength concrete at elevated temperatures, Cement and Concrete Research 42 (2012) 459–466. 10.1016/j.cemconres.2011.11.014.

[7] Y. Bu, B. Xue, Z. Huang, M. Yang, Z. Zhang, C. Zheng, Parameter inversion of the concrete hydration heat source based on physics-informed neural network, International Journal of Heat and Mass Transfer 260 (2026) 128409. 10.1016/j.ijheatmasstransfer.2026.128409.

[8] Y. Li, W. Liu, J. Ren, M. Cui, Z. Zhang, M. A. Nikolaitchik, An improved physics-informed neural network framework for solving transient nonlinear and inhomogeneous heat conduction problems, International Journal of Heat and Mass Transfer 252 (2025) 127515. 10.1016/j.ijheatmasstransfer.2025.127515.

[9] M.S. Bidou, J.-G. Bauzin, N. Laraqi, Physics-informed neural networks for 2D-transient inverse heat conduction problem involving static and moving heat source, International Journal of Heat and Mass Transfer 259 (2026) 128349. 10.1016/j.ijheatmasstransfer.2026.128349.

[10] J. Ozbolt, G. Periskic, H.-W. Reinhardt, R. Eligehausen, Numerical analysis of spalling of concrete cover at high temperature, Computers and Concrete 5 (2008) 279–293. 10.12989/cac.2008.5.4.279.

[11] J. Zhang, J. Chen, R. Zhang, R. Guo, A numerical investigation of thermal-induced explosive spalling behavior of a concrete material using cohesive interface model, Frontiers in Physics 10 (2022) 857381. 10.3389/fphy.2022.857381.

[12] L. Kong, Z. Fan, J. Lu, L. Zhang, Microstructure evolution of interfacial transition zone between alkali-activated fly ash/slag matrix and aggregate, Materials and Structures 55 (2022) 203. 10.1617/s11527-022-01938-4.

[13] M. Kashif, A. Naseem, K.C. Onyelowe, M.R. Riaz, S.S. Mehboob, P. De Winne, H. De Backer, Finite element modeling of active cracking in actively reinforced concrete pavement slab exposed to fluctuating temperature, Scientific Reports 14 (2024) 17337. 10.1038/s41598-024-68414-7.

[14] K. Chen, Y.-G. Zhao, S.-Q. Lin, Strength-grade-adaptive aggregate generation via multientropy-multifractal optimization for refined concrete FE modelling, Materials and Structures 59 (2026) 273. 10.1617/s11527-026-03162-w.

[15] B. Wu, X. Liang, F. Dang, B. Yang, T. Linghu, B. Hou, A novel mesoscale modeling approach and 3D thermal cracking phase field simulations for

concrete, Journal of Building Engineering (2025) 113938. 10.1016/j.jobe.2025.113938.

[16] J. Liu, Y. Liu, Z. Xie, X. Gong, Mesoscale numerical investigation of thermal conduction in recycled aggregate concrete, Journal of Building Engineering 129 (2026) 116835.

[17] D. Li, B. Sun, L. Yang, W. Wang, Mechanical and thermal properties of recycled coarse aggregate concrete incorporating microencapsulated phase change materials and recycled tire rubber granules and its freeze-thaw resistance, Journal of Building Engineering 101 (2025) 111821. 10.1016/j.jobe.2025.111821.

[18] A. Tordesillas, S. Kahagalage, C. Ras, M. Nitka, J. Tejchman, Early prediction of macrocrack location in concrete, rocks and other granular composite materials, Scientific Reports 10 (2020) 20268. 10.1038/s41598-020-76616-y.

[19] M. Mutnbak, A. Abbadi, S. Mousa, A.A. Abd-Elhady, H.E.-D.M. Sallam, R.M. Reda, Effects of specimen geometry and size on mode I and mixed mode fracture behavior of high strength fiber reinforced concrete, Scientific Reports 15 (2025) 15286. 10.1038/s41598-025-99013-9.

[20] G.-M. Ren, H. Wu, Q. Fang, X.-Z. Kong, Parameters of Holmquist–Johnson–Cook model for high-strength concrete-like materials under projectile impact, International Journal of Protective Structures 8 (2017) 352–367. 10.1177/2041419617721552.

[21] Z. Deng, B. Kuwik, T.C. Hufnagel, R.C. Hurley, Impact damage across length scales in concrete: Macro-, micro-, and nano-scale damage characterization, International Journal of Impact Engineering 215 (2026) 105763. 10.1016/j.ijimpeng.2026.105763.

[22] L. Yan, L. Chen, B. Chen, Q. Fang, Analysis and evaluation of suitability of high-pressure dynamic constitutive model for concrete under blast and impact loading, International Journal of Impact Engineering 195 (2025) 105145. 10.1016/j.ijimpeng.2024.105145.

[23] L. Ahmed, A. Ansell, R. Malm, Numerical modelling and evaluation of laboratory tests with impact loaded young concrete prisms, Materials and Structures 49 (2016) 4691–4704. 10.1617/s11527-016-0817-5.

[24] D. Sulsky, Z. Chen, H.L. Schreyer, A particle method for history-dependent materials, Computer Methods in Applied Mechanics and Engineering 118 (1994) 179–196. 10.1016/0045-7825(94)90112-0.

[25] D. Sulsky, S.-J. Zhou, H.L. Schreyer, Application of a particle-in-cell method to solid mechanics, Computer Physics Communications 87 (1995) 236–252. 10.1016/0010-4655(94)00170-7.

[26] A. de Vaucorbeil, V.P. Nguyen, S. Sinaie, J.Y. Wu, Material point method after 25 years: Theory, implementation, and applications, in: Advances in Applied Mechanics, vol. 53, 2020, pp. 185–398. 10.1016/bs.aams.2019.11.001.

[27] M. Steffen, R.M. Kirby, M. Berzins, Analysis and reduction of quadrature errors in the material point method (MPM), International Journal for Numerical Methods in Engineering 76 (2008) 922–948. 10.1002/nme.2360.

[28] M. Steffen, P.C. Wallstedt, J.E. Guilkey, R.M. Kirby, M. Berzins, Examination and analysis of implementation choices within the material point method (MPM), Computer Modeling in Engineering & Sciences 31 (2008) 107–127. 10.3970/cmes.2008.031.107.

[29] S.G. Bardenhagen, E.M. Kober, The generalized interpolation material point method, Computer Modeling in Engineering & Sciences 5 (2004) 477–495. 10.3970/cmes.2004.005.477.

[30] A. Sadeghirad, R.M. Brannon, J. Burghardt, A convected particle domain interpolation technique to extend applicability of the material point method for problems involving massive deformations, International Journal for Numerical Methods in Engineering 86 (2011) 1435–1456. 10.1002/nme.3110.

[31] A. Sadeghirad, R.M. Brannon, J.E. Guilkey, Second-order convected particle domain interpolation (CPDI2) with enrichment for weak discontinuities at material interfaces, International Journal for Numerical Methods in Engineering 95 (2013) 928–952. 10.1002/nme.4526.

[32] Y. Gan, Z. Sun, Z. Chen, X. Zhang, Y. Liu, Enhancement of the material point method using B-spline basis functions, International Journal for Numerical Methods in Engineering 113 (2018) 411–431. 10.1002/nme.5620.

[33] A. de Vaucorbeil, V.P. Nguyen, C.R. Hutchinson, A Total-Lagrangian Material Point Method for solid mechanics problems involving large deformations, Computer Methods in Applied Mechanics and Engineering 360 (2020) 112783. 10.1016/j.cma.2019.112783.

[34] R.M. Telikicherla, G. Moutsanidis, An assessment of the total Lagrangian material point method: Comparison to conventional MPM, higher order basis, and treatment of near-incompressibility, Computer Methods in Applied Mechanics and Engineering 414 (2023) 116135. 10.1016/j.cma.2023.116135.

[35] A. de Vaucorbeil, V.P. Nguyen, Modelling contacts with a total Lagrangian material point method, Computer Methods in Applied Mechanics and Engineering 373 (2021) 113503. 10.1016/j.cma.2020.113503.

[36] Z. Zhang, Y. Qiu, Z. Hu, H. Ye, H. Zhang, Y. Zheng, Explicit phase-field total Lagrangian material point method for the dynamic fracture of hyperelastic materials, Computer Methods in Applied Mechanics and Engineering 398 (2022) 115234. 10.1016/j.cma.2022.115234.

[37] Y. Zheng, S. Zhang, W. Yang, Z. Zhang, H. Ye, H. Zhang, Adaptive phase-field total Lagrangian material point method for evaluating dynamic fracture of soft material, Engineering with Computers 41 (2025) 1411–1434. 10.1007/s00366-024-02019-6.

[38] J. Tao, Y. Zheng, Z. Chen, H. Zhang, Generalized interpolation material point method for coupled thermo-mechanical processes, International Journal of Mechanics and Materials in Design 12 (2016) 577–595. 10.1007/s10999-016-9339-0.

[39] W. Lee, D. Shin, Thermomechanical modeling in elastic body with corotated total Lagrangian SPH, Computers & Structures 301 (2024) 107428. 10.1016/j.compstruc.2024.107428.

[40] H. Xu, C. Wang, H. Jia, Z. Liu, M. Wan, Z. Zhang, Y. Zheng, Enhanced physics-informed neural networks without labeled data for weakly and fully coupled transient thermomechanical analysis, International Journal of Solids and Structures 305 (2024) 113092. 10.1016/j.ijsolstr.2024.113092.

[41] J.C. Simo, C. Miehe, Associative coupled thermoplasticity at finite strains: Formulation, numerical analysis and implementation, Computer Methods in Applied Mechanics and Engineering 98 (1992) 41–104. 10.1016/0045-7825(92)90170-O.

[42] H. Htike, W. Chen, Y. Gu, J. Yang, Material point method with RBF interpolation, Computer Modeling in Engineering & Sciences 72 (2011) 247–272. 10.3970/cmes.2011.072.247.

[43] D.Z. Zhang, X. Ma, P.T. Giguere, Material point method enhanced by modified gradient of shape function, Journal of Computational Physics 230 (2011) 6379–6398. 10.1016/j.jcp.2011.04.032.

[44] D.Z. Zhang, T.R. Dhakal, Shock waves simulated using the dual domain material point method combined with molecular dynamics, Journal of Computational Physics 334 (2017) 240–254. 10.1016/j.jcp.2017.01.003.

[45] Z. Sun, X. Zhou, An efficient particle subdomain quadrature scheme for the material point method, Acta Mechanica Solida Sinica 34 (2021) 274–285. 10.1007/s10338-020-00190-z.

[46] K. Zhang, R. Cen, S. Zhu, R. Chen, B. Ren, DIQ-MPM: Dual interface quadrature MPM for simulating large deformation and fluid-solid coupling, IEEE Transactions on Visualization and Computer Graphics 32 (2026) 5803–5814. 10.1109/TVCG.2026.3674656.

[47] Y. Liang, X. Zhang, Y. Liu, An efficient staggered grid material point method, Computer Methods in Applied Mechanics and Engineering 352 (2019) 85–109. 10.1016/j.cma.2019.04.024.

[48] L. Kan, Y. Liang, X. Zhang, A critical assessment and contact algorithm for the staggered grid material point method, International Journal of Mechanics and Materials in Design 17 (2021) 743–766. 10.1007/s10999-021-09557-7.

[49] J.-U. Song, H.-G. Kim, An implicit material point method using a cell-based integration scheme for large deformation static problems, Computational Particle Mechanics 11 (2024) 1959–1979. 10.1007/s40571-024-00720-3.

[50] Z. Sun, H. Li, Y. Gan, H. Liu, Z. Huang, L. He, Material point method and smoothed particle hydrodynamics simulations of fluid flow problems: a comparative study, Progress in Computational Fluid Dynamics, An International Journal 18 (2018) 1–18. 10.1504/PCFD.2018.089497.

[51] Z. Wang, G. Wang, F. Han, A mixed-formulated total Lagrangian material point method for dynamic interaction between structure and soil, Computers and Geotechnics 180 (2025) 107047. 10.1016/j.compgeo.2024.107047.

[52] S. Nezamabadi, F. Radjai, Explicit total Lagrangian material point method with implicit frictional-contact model for soft granular materials, Granular Matter 26 (2024) 67. 10.1007/s10035-024-01438-y.

[53] S. Zhou, G. Chen, L. Qian, J. Ma, HLFEMP: A coupled MPM-FEM method under a hybrid updated and total Lagrangian framework, Applied Mathematical Modelling 136 (2024) 115644. 10.1016/j.apm.2024.115644.